Inferences on ultralow-velocity zone structure from a global analysis of *SPdKS* waves

Michael S. Thorne and Edward J. Garnero

Department of Geological Sciences, Arizona State University, Tempe, Arizona, USA

Received 5 February 2004; revised 10 May 2004; accepted 7 June 2004; published 4 August 2004.

[1] Anomalous boundary layer structure at the core-mantle boundary (CMB) is investigated using a global set of broadband *SKS* and *SPdKS* waves from permanent and portable broadband seismometer arrays. *SPdKS* is an *SKS* wave that intersects the CMB at the critical angle for *ScP*, thus initiating a diffracted *P* wave (P_{diff}) along the CMB at the core entry and exit locations. The waveshape and timing of *SPdKS* data are analyzed relative to *SKS*, with some *SPdKS* data showing significant delays and broadening. Broadband data from several hundred deep focus earthquakes were analyzed; retaining data with simple sources and high signal-to-noise ratios resulted in 53 high-quality earthquakes. For each earthquake an empirical source was constructed by stacking pre-*SPdKS* distance range *SKS* pulses ($\sim$90°–100°). These were utilized in our synthetic modeling process, whereby reflectivity synthetic seismograms are produced for three classes of models: (1) mantle-side ultralow-velocity zones (UVLZ), (2) underside CMB core rigidity zones, and (3) core-mantle transition zones. For ULVZ structures, ratios of *P*-to-*S* velocity reductions of 1:1 and 1:3 are explored, where 1:3 is appropriate for a partial melt origin of ULVZ. Over 330 unique CMB boundary layer models have been constructed and tested, corroborating previous work suggesting strong trade-offs between the three model spaces. We produce maps of inferred boundary layer structure from the global data and find evidence for extremely fine-scale heterogeneity where our wave path sampling is the densest. While uncertainties are present relating to the source versus receiver sides of the *SPdKS* wave path geometry, our data are consistent with the hypothesis that ULVZ presence (or absence) correlates with reduced (or average) heterogeneity in the overlying mantle. *INDEX TERMS:* 7207 Seismology: Core and mantle; 8120 Tectonophysics: Dynamics of lithosphere and mantle—general; 8121 Tectonophysics: Dynamics, convection currents and mantle plumes; 8115 Tectonophysics: Core processes (1507); *KEYWORDS:* ultralow-velocity zone, core-mantle boundary

Citation: Thorne, M. S., and E. J. Garnero (2004), Inferences on ultralow-velocity zone structure from a global analysis of *SPdKS* waves, *J. Geophys. Res.*, *109*, B08301, doi:10.1029/2004JB003010.

1. Introduction

[2] Evidence for strong *P* and *S* wave velocity reductions at the core-mantle boundary (CMB) has been reported for over two decades. Here we briefly summarize these past efforts, from early CMB heterogeneity and tomography studies to more recent work specifically aimed at characterization of ultralow-velocity zone (ULVZ) structure, and then discuss the geographic distribution and possible origin of ULVZs presented in past work. This provides the basis for the work we report in this paper.

1.1. Early Indirect Evidence for ULVZ: CMB Topography Studies

[3] The first studies reporting strong velocity reductions as well as lateral variations at the CMB were aimed at resolving CMB topography. For example, models of CMB topography derived from the inversion of core phases that cross or reflect off of the CMB (e.g., *PKP*, *PcP*) map CMB undulations of up to ±10 km [e.g., *Creager and Jordan*, 1986; *Morelli and Dziewonski*, 1987]. Additionally, travel time variations of core-reflected *PcP* waves referenced to *PKP* have suggested CMB topography as large as ±15 km [e.g., *Rodgers and Wahr*, 1993]. Consensus on the exact distribution or patterns of CMB topography, as well as peak-to-peak topography amplitude, is lacking at present [e.g., *Rodgers and Wahr*, 1993; *Garcia and Souriau*, 2000], and subsequent identification of thin zones of ultralow velocities further complicates efforts to constrain CMB topography because of the strong trade-off between volumetric heterogeneity and CMB topography. Peak-to-peak amplitudes of CMB topography inferred from seismic studies (up to ±15 km) are considerably larger than those from dynamical considerations (roughly ±0.5–3 km) [e.g., see *Hager et al.*, 1985; *Bowin*, 1986; *Hide et al.*, 1993].

0148-0227/04/2004JB003010$09.00

This discrepancy may, in fact, be due to a mismapping of ULVZ signal. We note that the likely existence of CMB topography does not strongly contaminate ULVZ studies.

[4] Volumetric heterogeneity in the D″ region may help reconcile discrepancies in mapped CMB peak-to-peak amplitudes. By observing the amplitude decay of long-period P_{diff} and S_{diff} and short-period P_{diff}, *Doornbos* [1983] concluded that the CMB might have significant lateral variations within a relatively thin (<100 km) low-velocity boundary layer. Subsequently, *Doornbos and Hilton* [1989] inverted *PcP*, *PKP*, and *PnKP* for CMB topography to support relatively reduced CMB topography (±4 km) and argued that lateral variations in travel time residuals of *PcP* and *PKP* can be best modeled by a laterally varying lowermost mantle boundary layer (in the form of variable layer thickness, velocity fluctuations, or some combination of the two), with average layer thickness of ∼20 km, and *P* wave velocity heterogeneity perturbations up to ±7.3%. While the thickness of their solution layer is not well constrained because there is a direct trade-off with velocity heterogeneity in the layer, the inference for thin zones of strong reductions was made. A recent demonstration of this trade-off arose in a joint inversion for peak-to-peak topography and D″ heterogeneity using the seismic phases *PcP*, *PKP*, and *PKKP*: *Sze and van der Hilst* [2003] found that ±13 km CMB undulations are necessary if no D″ velocity variations are invoked. This reduces to CMB topography amplitude of ±3 km if ±5% D″ variations (lowermost 290 km) in *P* wave velocities are considered. Further evidence for this trade-off was reported by *Garcia and Souriau* [2000]; they present evidence for peak-to-peak topography from 1.5 to 4.0 km with lateral scales of 300–1500 km. These recent models are in greater agreement with dynamical models in terms of peak-to-peak topography values. We note that shorter-scale CMB topography or roughness may be superimposed on this longer-wavelength CMB topography [*Earle and Shearer*, 1997; *Shearer et al.*, 1998; *Garcia and Souriau*, 2000].

[5] A multitude of studies over the last 15–20 years have put forth evidence for strong deep mantle heterogeneity. These efforts may have similarly mapped ULVZ signal into larger-scale D″ heterogeneity. This may be especially relevant for lower mantle structure from tomographic studies. Currently, the highest-resolution modeling efforts have presented heterogeneity at lateral and vertical scales on the order of 500+ km [e.g., *Masters et al.*, 2000; *Megnin and Romanowicz*, 2000; *Grand*, 2002]. Small-scale ULVZ structure likely maps into these velocity predictions, though to what extent is extremely difficult to assess because it is quite likely that strong D″ heterogeneity exists in addition to ULVZ structure (see, for example, review by *Garnero* [2000]).

1.2. Recent Probes of ULVZ Structure

[6] Recent efforts have been aimed at looking directly for ULVZ structure. A summary of these studies is provided in Table 1. The probes used can be organized as follows: precursors to the core-reflected phases *PcP* and *ScP*, scattering from the core wave *PKP*, and travel time and/or waveform anomalies of a variety of mantle and core waves, including *ScS*, *SPdKS*, *PcP*, and *PKP*.

[7] Analysis of precursors to the core-reflected phases *PcP* and *ScP* has proven extremely valuable in mapping detailed structure of boundary layer structure at the CMB. These studies have predominantly utilized short-period array data, revealing a wide variety of observations from a simple CMB with no evident precursors [*Vidale and Benz*, 1992; *Castle and van der Hilst*, 2000] to highly anomalous zones characterized as ULVZ or thin core-side layering with finite rigidity (a "core-rigidity zone," or CRZ) with small-scale lateral variations on the order of tens of kilometers [e.g., *Garnero and Vidale*, 1999; *Rost and Revenaugh*, 2001, 2003]. These studies also highlight apparent contradictions in some geographic locales where evidence for and against anomalous boundary layer structure has been put forth. For example, using short-period *PcP* stacks, *Mori and Helmberger* [1995] and *Revenaugh and Meyer* [1997] both observed precursors in the central Pacific that indicated the presence of a ULVZ. However, these two studies disagree as to whether a ULVZ exists in a location in the east Pacific. The recent use of broadband data is helping to reconcile these contradictions, as well as to better constrain the limits on sharpness of the structural features responsible for precursors [*Havens and Revenaugh*, 2001; *Rondenay and Fischer*, 2003].

[8] Small-scale scatterers in D″ can give rise to *PKP* precursors and have also been used to map anomalous ULVZ and CMB structure [e.g., *Vidale and Hedlin*, 1998; *Wen and Helmberger*, 1998b]. *PKP* precursors attributed to ULVZ structure have been observed in short-period, long-period, and broadband data (see Table 1). The presence of short- and long-period *PKP* precursors in data from a given region can be attributed to variable scatterer scale lengths, from tens of kilometers up to 100–300 km [*Wen and Helmberger*, 1998b]. Additionally, migration techniques have been employed to locate scatterers with scale lengths of ∼10–50 km [*Thomas et al.*, 1999]. The presence of large *S* wave velocity reductions relative to *P* wave reductions, as predicted by the partial melt origin of the ultralow velocities [*Williams and Garnero*, 1996; *Berryman*, 2000], produces observable *SKS* precursors for ULVZ layer thickness greater than ∼15 km (if velocity reductions are 10 and 30% for *P* and *S*, respectively). However, these have not yet been identified or documented [*Stutzmann et al.*, 2000]. Such precursors would go undetected if either (1) partial melt layering is thinner than 10–15 km or (2) the *P* and *S* wave reductions are less than 10 and 30%, respectively, such as 5 and 15% or less.

[9] In addition to studying precursors a wide variety of studies have inferred ULVZ presence from differential travel time and waveform anomalies of *SPdKS* waves referenced to *SKS* (Table 1). One advantage in using *SPdKS* is greatly increased global sampling. However, inherent trade-offs exist in constraining ULVZ elastic parameters as well as geographic location, which are discussed in detail in this paper. Additionally, travel time and waveform studies of *ScS* relative to *S* have proven significant in revealing ULVZ structure in regions not sampled by *SPdKS* [*Simmons and Grand*, 2002; *Ni and Helmberger*, 2003b].

1.3. Geographic Distribution of ULVZ

[10] Most ULVZ studies have utilized the abundance of deep focus earthquakes from the Pacific rim, which has resulted in CMB structure beneath three areas being extensively studied: (1) the southwest Pacific, (2) Central Amer-

Table 1. Core-Mantle Boundary Layer Studies

Study	Reference	Phases Used[a]	Region	Sighting[b]
		Precursors to Core Reflected Phases		
1	*Vidale and Benz* [1992]	SP *ScP* stacks	NE Pacific	N
2	*Mori and Helmberger* [1995]	SP *PcP* stacks	central, east Pacific	Y, N
3	*Kohler et al.* [1997]	SP *PcP* stacks	central Pacific	Y, N
4	*Revenaugh and Meyer* [1997]	SP *PcP* stacks	central, east, NE Pacific	Y
5	*Garnero and Vidale* [1999]	SP, BB *ScP*	SW Pacific	Y, N
6	*Castle and van der Hilst* [2000]	SP, BB *ScP*	NE Pacific, Central America	N
7	*Reasoner and Revenaugh* [2000]	SP *ScP* stacks	SW Pacific	Y, N
8	*Havens and Revenaugh* [2001]	BB *PcP* stacks	central Mexico, western Gulf of Mexico	Y, N
9	*Persh et al.* [2001]	SP *PcP, ScP* stacks	NE Pacific, Central America	N
10	*Rost and Revenaugh* [2001]	SP *ScP* stacks	SW Pacific	Y
11	*Rost and Revenaugh* [2003]	SP *ScP* stacks	SW Pacific	Y, N
		Scattered Core Phases		
12	*Vidale and Hedlin* [1998]	SP *PKP* precursors	SW Pacific	Y
13	*Wen and Helmberger* [1998b]	SP, LP *PKP* precursors	SW Pacific	Y
14	*Thomas et al.* [1999]	BB *PKP* precursors	SW Pacific, northern Europe	Y
15	*Wen* [2000]	BB *PKP* precursors	underneath Comores	Y
16	*Stutzmann et al.* [2000]	BB *SKS* precursors	SW Pacific	N
17	*Ni and Helmberger* [2001a]	BB *PKP* precursors, *SKPdS*	western Africa	Y
18	*Niu and Wen* [2001]	SP *PKP* precursors	west of Mexico	Y
		Travel Time and Waveform Anomalies		
19	*Garnero et al.* [1993]	LP *SPdKS*	central Pacific	Y
20	*Garnero and Helmberger* [1995]	LP *SPdKS*, *SKS*, SV_{diff}	Pacific, North America	Y, N
21	*Garnero and Helmberger* [1996]	LP *SPdKS*	central, circum-Pacific	Y, N
22	*Helmberger et al.* [1996]	SP, LP *SPdKS*	central Pacific	Y
23	*Garnero and Helmberger* [1998]	LP *SPdKS*	central Pacific, circum-Pacific	Y, N
24	*Helmberger et al.* [1998]	LP *SPdKS*	Iceland	Y
25	*Wen and Helmberger* [1998a]	LP *SPdKS*	SW Pacific	Y
26	*Bowers et al.* [2000]	BB *PKPdf, PKPbc*	SW Pacific, east of Iceland	Y
27	*Helmberger et al.* [2000]	LP *SPdKS*	Africa, east Atlantic	Y
28	*Luo et al.* [2001]	BB *PKPab-PKPdf*	central Pacific	Y
29	*Ni and Helmberger* [2001b]	BB *S,ScS*	South Atlantic	Y
30	*Wen* [2001]	BB *S, ScS,* SH_{diff}, P_{diff}, *SKS*	Indian Ocean	Y
31	*Simmons and Grand* [2002]	BB *ScS-S, PcP-P*	South Atlantic	Y
32	*Ni and Helmberger* [2003b]	LP, BB *SKS-S, ScS-S*	south Africa	Y
33	*Rondenay and Fischer* [2003]	BB *SKS* coda	North America	Y

[a]SP, short period; LP, long period; BB, broadband.
[b]Y, yes; N, no.

ica, and (3) the northeast Pacific. Figure 1 summarizes the results of previous studies under the southwest Pacific and Central America regions. The southwest Pacific region is dominated by a large low-velocity anomaly prominent in models of shear wave tomography [e.g., see *Masters et al.*, 2000] and may also contain the source of several hot spots [e.g., see *Sleep*, 1990; *Steinberger*, 2000; *Montelli et al.*, 2004; *Thorne et al.*, 2004]. In contrast to this, the Central America region may be home to remnants of the subducted Farallon slab as indicated by relatively high shear wave velocities [e.g., *Grand et al.*, 1997]. Evidence for a small-scale, high-attenuation, low-velocity anomaly has also been put forth for the Caribbean region [*Wysession et al.*, 2001; *Fisher et al.*, 2003], as well as short-scale lateral heterogeneity [*Tkalčić and Romanowicz*, 2002]. Additionally, the source of the Galapagos, Guadelupe, and Socorro hot spots may lie in the west of this region. Lightly shaded patches represent *SPdKS* Fresnel zones: pink shading denotes ULVZ detection and light blue shading indicates that no ULVZ was detected [*Garnero et al.*, 1998]. These zones predominantly characterize long-wavelength structure. Shorter scale length ULVZ phenomena are provided from core reflected precursors or scattering studies: a high degree of variability is observed, as can be seen in the southwest Pacific (symbols and lines in Figure 1a). For example, observations of *ScP* precursors that indicate anomalous boundary layer structure are colocated with normal *ScP* waveforms [*Garnero and Vidale*, 1999; *Reasoner and Revenaugh*, 2000; *Rost and Revenaugh*, 2001, 2003]. Disagreement between the long-wavelength ULVZ map [*Garnero et al.*, 1998] and the short-scale results shown in Figure 1 are due to (1) ULVZ heterogeneity existing at wavelengths shorter than *SPdKS* Fresnel zones, (2) uncertainties due to the source-receiver-side ambiguity of the source of *SPdKS* anomalies (which we address in sections 6.2 and 6.3), and (3) possible sensitivity to different ULVZ structure features.

1.4. Origin of ULVZ Anomalies

[11] Several explanations have been proposed for the origin of ULVZ structure. These fall into the categories of (1) chemically unique material on the mantle side of the CMB [e.g., *Manga and Jeanloz*, 1996; *Stutzmann et al.*, 2000], (2) partial melt of some component of the lowermost mantle right at/above the CMB [e.g., *Williams and Garnero*, 1996; *Revenaugh and Meyer*, 1997; *Helmberger et al.*, 1998; *Vidale and Hedlin*, 1998; *Williams et al.*, 1998; *Zerr et al.*, 1998; *Berryman*, 2000; *Wen*, 2000], (3) material with finite rigidity pooling at the underside of the CMB, for example, beneath CMB topographical highs [e.g., *Buffett et al.*, 2000;

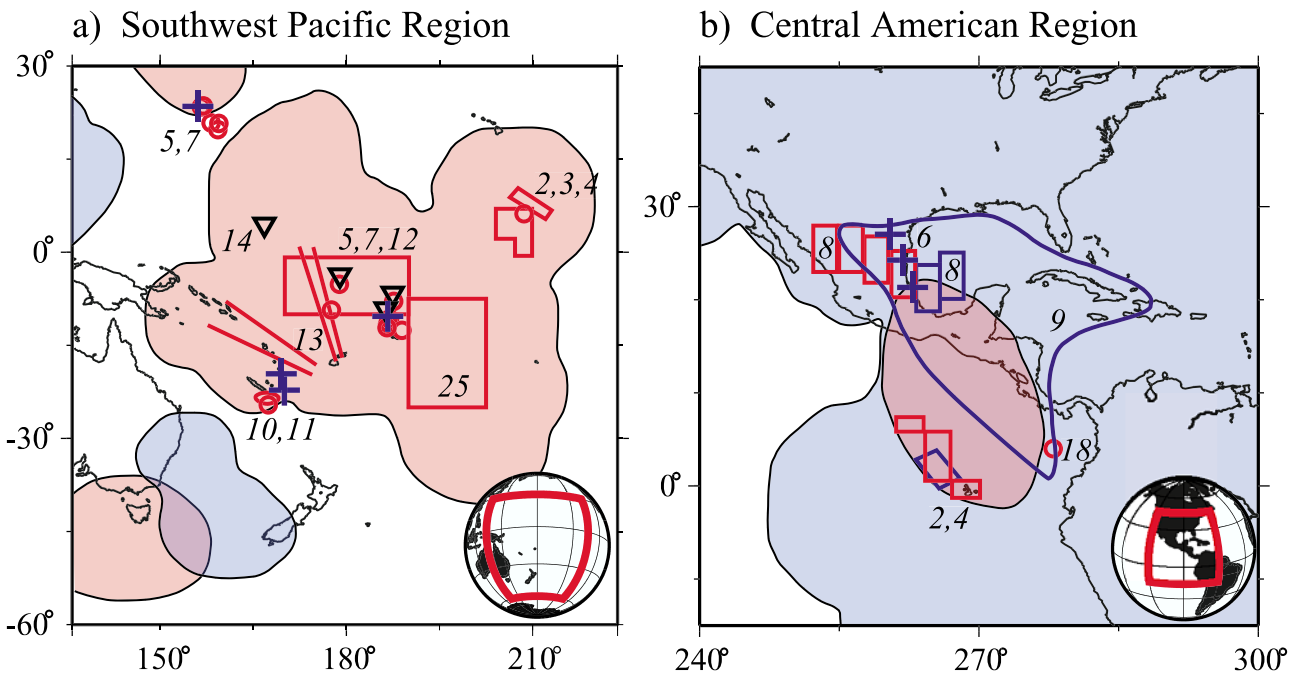

Figure 1. Past study results for (a) southwest Pacific and (b) Central America regions of the CMB, respectively. The light red and blue shaded regions correspond to areas where ULVZ have and have not been previously detected [*Garnero et al.*, 1998]. Red boxes, lines, and circles correspond to locations where anomalous boundary layer structure has been inferred from previous studies as outlined in Table 1 (numbers correspond to those of Table 1). Blue boxes, crosses, and outlined regions correspond to locations where anomalous boundary layer structure has previously been searched for but not observed. Black triangles correspond to locations where anomalous boundary layer structure may exist, yet data are inconclusive.

Rost and Revenaugh, 2001], (4) some form of blurring of the CMB, such as a transition between core and mantle material from some form of mixing or chemical reactions [*Garnero and Jeanloz*, 2000a, 2000b], and (5) any combination of the above [*Rost and Revenaugh*, 2001]. Increased resolution is necessary for better characterization of boundary layer structure at the CMB. This is additionally important as it may relate to the source regions of whole mantle plumes responsible for hot spot volcanism [*Williams et al.*, 1998], the frequency of magnetic field reversals [*Glatzmaier et al.*, 1999], and nutation of Earth's rotation axis [*Buffett et al.*, 2000]. At a minimum, the patches or zones of ultralow velocities are likely related to deep mantle dynamics and chemistry. To more accurately constrain elastic properties of boundary layer structure at the CMB, we improve CMB coverage in this paper as sampled by broadband *SPdKS* data, which we hope can contribute to future analyses using the various other probes (e.g., Table 1).

2. *SPdKS* Data

[12] This study utilizes a global set of broadband *SPdKS* data. *SPdKS* is an *SKS* wave, where the downgoing *S* wave intersects the CMB at the critical angle for diffraction generating *P*-diffracted (P_{diff}) segments propagating on the mantle side of the CMB. The complementary phase *SKPdS* has the P_{diff} leg occurring on the receiver side, where the upgoing *P* wave intersects the CMB at the critical angle. For the preliminary reference Earth model (PREM) [*Dziewonski and Anderson*, 1981], *SPdKS* initiates at ~104°; however, the bifurcation between *SKS* and *SPdKS* is not observable in broadband waveforms until ~110°. Ray path geometries are shown for four distances in Figure 2 (top), with both *SPdKS* and *SKPdS* being displayed. As the source-receiver distance increases, the length of P_{diff} segments on the CMB increases, which is the only alteration to *SPdKS*+*SKPdS* paths with distance. For example, for PREM, P_{diff} segments are 420 and 1000 km for 110° and 120° source-receiver distances, respectively (see Figure 2, middle). The distance between the core entry (exit) locations of *SKS* and *SPdKS* (*SKPdS*) at the CMB also increases with distance. For example, for PREM the *SKS* − *SPdKS* separation increases from 60 to 210 km for a source-receiver distance increase of 110° to 120° (see Figure 2, middle). Example synthetic seismograms (for PREM) for the four distances are shown in Figure 2 (bottom). Data with source-receiver distances of 110°−115° are most useful as strong waveform distortions are observed, particularly near 110° where interference with *SKS* results in diagnostic waveform shapes. Source-receiver geometries with distances of near 120° (and greater) have broader *SPdKS* pulses due to long P_{diff} segments. These are less useful for modeling detailed short-scale ULVZ structure because CMB and D″ structure is averaged over fairly large distances. If the mantle structure encountered on both the source- and receiver-side CMB crossing location is identical, *SPdKS* and *SKPdS* have coincident arrival times. However, differing source- and receiver-side mantle structure should affect the timing, amplitude, and waveshape of

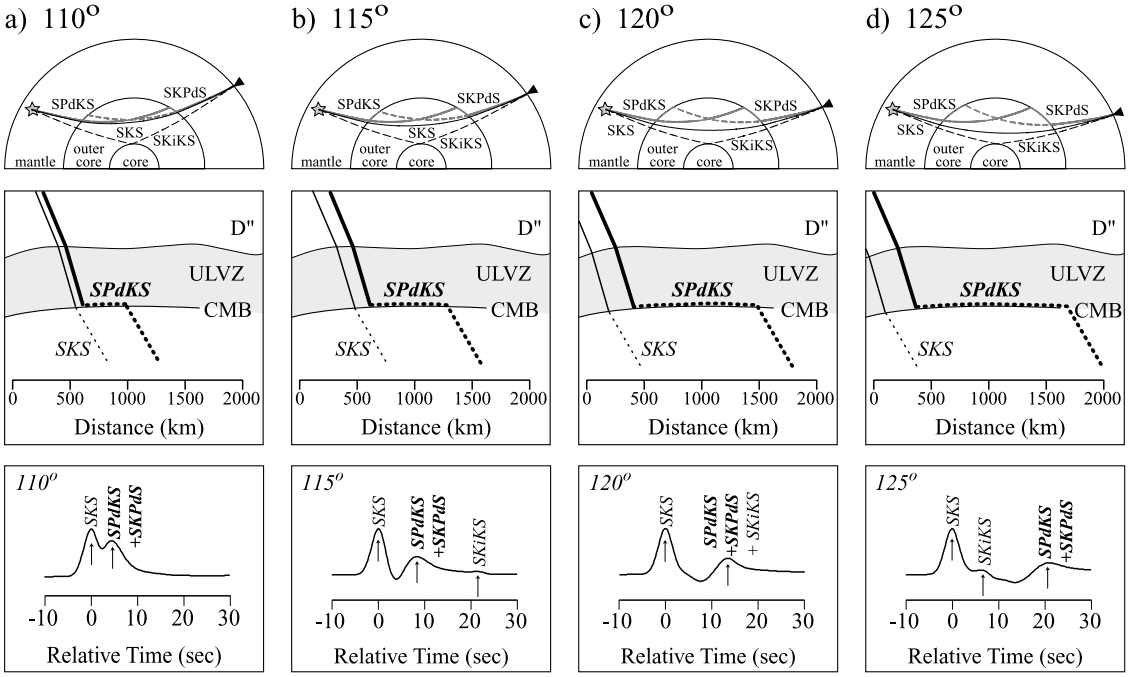

Figure 2. Phases used in this study at four epicentral distances. (top) Ray paths for *SKS*, *SPdKS* (both *SPdKS* and *SKPdS*), and *SKiKS*. (middle) Enlarged ray path of *SKS* and *SPdKS* for each distance. The lateral distance along the CMB of the P_{diff} portion of *SPdKS* is shown as is the amount of lateral separation between *SKS* and *SPdKS* (calculated for the PREM model), with the vertical scale exaggerated. (bottom) PREM synthetic seismograms highlighting the arrivals at each distance.

SPdKS and *SKPdS* [e.g., *Rondenay and Fischer*, 2003]. Yet, it is not generally possible to distinguish *SPdKS* from *SKPdS* in observed waveforms. We note one recent array analysis using the phase-stripping method of eigenimage decomposition has been able to separately identify the source and receiver contributions to the combined wave fields [*Rondenay and Fischer*, 2003]. For convenience, the combined *SPdKS* plus *SKPdS* energy is referred to as *SPdKS* throughout this paper.

[13] Figure 2 also shows the phase *SKiKS*, which is an *SKS* wave that reflects off the inner core boundary (ray path geometry shown in Figure 2, top). Figure 2 (bottom) shows the *SKiKS* arrival at four distances. Most notably, for the PREM model, *SKiKS* arrives coincident with *SPdKS* at a distance of ~120° and may interfere with the *SPdKS* arrival.

[14] Data used in this study were collected from the publicly available Incorporated Research Institutions for Seismology Data Management Center (IRIS DMC). Initially, we conducted a global search for earthquakes using IRIS's Fast Archive Recovery Method (FARM) catalog. We searched for earthquakes with depths greater than 100 km, and moment magnitudes (M_w) greater than 6.0, for events occurring between 1990 and 2000. This resulted in a collection of 321 events. To further augment our data set, we also obtained broadband data for several earthquakes from the Observatories and Research Facilities for European Seismology (ORFEUS) Data Center (ODC), the Canadian National Seismic Network (CNSN), and PASSCAL data available from the IRIS DMC.

[15] All data were instrument deconvolved to displacement using the Seismic Analysis Code (SAC) [*Goldstein et al.*, 1999] transfer function, and the pole-zero response files obtained from the IRIS DMC, with a band-pass window from 0.01 to 1.0 Hz. Resultant displacement files were then rotated to great circle path radial and transverse components and resampled to a 0.1 s time interval. We retained radial component seismograms for analysis of *SPdKS* relative to *SKS*.

[16] All data were visually inspected to determine data quality; initial criteria leading to data rejection were (1) no stations were located in the epicentral distance range of 90°–125° or (2) it was not possible to clearly distinguish the seismic phase *SKS* above the background noise level. Using these criteria, the number of events reduced from 321 to 53. In total, records were examined for 182 unique stations in the distance range 105°–125°, resulting in 443 unique records used in this study. Table 2 displays the resulting 53 events used in this study. The most notable CMB sampling is beneath the southwest Pacific, the Americas, eastern Eurasia, northern Africa and Europe, and the southern Indian Ocean.

[17] A distance profile for each event was visually inspected for possible anomalous source structure effects, where events with exceedingly complex sources were discarded. Profiles for four events used in this study are displayed in Figure 3. All traces are normalized in time and amplitude to the *SKS* peak (solid line at 0 s). The dashed and dotted lines show predicted arrivals for *SPdKS* and *SKiKS*, respectively, using the PREM model. Clean and impulsive *SKS* can be observed in these profiles for records from 100° to 110°, with the exception of the highly anomalous records in Figure 3d at stations CCM, FFC, TIXI, and WMQ (Cathedral Caves, Missouri; Flin Flon, Canada; Tiksi, Russia; and Urumqi, Xinjiang, China). These

Table 2. Earthquakes Used in This Study

Event	Date	Latitude, deg	Longitude, deg	Depth, km	M_w
1	20 May 1990	−18.1	−175.3	232	6.3
2	8 June 1990	−18.7	−178.9	209	6.9
3	7 June 1991	−7.3	122.6	563	6.9
4	23 June 1991	−26.8	−63.4	581	7.3
5	2 Aug. 1992	−7.1	121.7	483	6.6
6	8 Oct. 1992	−6.3	130.2	109	6.2
7	21 March 1993	−18.0	−178.5	584	6.3
8	9 July 1993	−19.8	−177.5	412	6.1
9	7 Aug. 1993	26.5	125.6	158	6.4
10	7 Aug. 1993	−23.9	179.8	555	6.7
11	11 Feb. 1994	−18.8	169.2	204	6.9
12	31 March 1994	−22.0	−179.6	591	6.5
13	29 April 1994	−28.3	−63.2	573	6.9
14	10 May 1994	−28.5	−63.1	605	6.9
15	13 July 1994	−7.5	127.9	185	6.5
16	19 Aug. 1994	−26.6	−63.4	565	6.5
17	29 June 1995	−19.5	169.2	144	6.6
18	14 Aug. 1995	−4.8	151.5	126	6.3
19	23 Aug. 1995	18.9	145.2	596	7.1
20	18 Sept. 1995	−6.95	128.9	180	6.0
21	6 Oct. 1995	−20.0	−175.9	209	6.4
22	25 Dec. 1995	−6.9	129.2	150	7.1
23	22 Feb. 1996	45.2	148.6	133	6.3
24	17 March 1996	−14.7	167.3	164	6.7
25	2 May 1996	−4.6	154.8	500	6.6
26	27 Aug. 1996	−22.6	−179.8	575	6.0
27	5 Nov. 1996	−31.2	180.0	369	6.8
28	1 Dec. 1996	−30.5	−179.7	356	6.1
29	22 Dec. 1996	43.2	138.9	227	6.5
30	21 March 1997	−31.2	179.6	449	6.3
31	11 June 1997	−24.0	−177.5	164	5.8
32	4 Sept. 1997	−26.6	178.3	625	6.8
33	28 Nov. 1997	−13.7	−68.8	586	6.7
34	27 Jan. 1998	−22.4	179.0	610	6.5
35	29 March 1998	−17.5	−179.1	537	7.2
36	3 April 1998	−8.1	−74.2	165	6.6
37	14 April 1998	−23.8	−179.9	499	6.1
38	16 May 1998	−22.2	−179.5	586	6.9
39	9 July 1998	−30.5	−179.0	130	6.9
40	8 Oct. 1998	−16.1	−71.4	136	6.2
41	11 Oct. 1998	−21.0	−179.1	624	5.9
42	27 Dec. 1998	−21.63	−176.4	144	6.8
43	8 April 1999	43.6	130.4	566	7.1
44	9 April 1999	−26.4	178.2	621	6.2
45	13 April 1999	−21.4	−176.5	164	6.8
46	26 April 1999	−1.6	−77.8	173	6.1
47	12 May 1999	43.0	143.8	103	6.2
48	17 Sept. 1999	−13.8	167.2	197	6.3
49	18 April 2000	−20.7	−176.5	221	6.0
50	14 June 2000	−25.5	178.1	605	6.5
51	16 June 2000	−33.9	−70.1	120	6.4
52	15 Aug. 2000	−31.5	179.7	358	6.6
53	18 Dec. 2000	−21.2	−179.1	628	6.6

anomalous records may be attributable to CMB structure, as the anomalous waveform behavior is not observed in other traces for the same event, as long as site effects can also be ruled out. Beyond 110°, the separation of *SPdKS* from *SKS* becomes apparent. *SPdKS* often arrives as predicted by PREM, however, several delayed *SPdKS* arrivals are also observed. Additionally, Figure 3 displays several smaller peaks having arrivals coincident with the PREM prediction for *SKiKS*, which is highly suggestive of *SKiKS* interference (or contamination) with the *SKS* and *SPdKS* arrivals.

[18] To determine if site effects are contributing to anomalous waveforms, *SPdKS* behavior at individual stations has been studied. Figure 4 shows distance profiles for four broadband stations. Three extremely anomalous records are seen for station CCM around 107° (Figure 4a). These anomalous traces show *SPdKS* (right shoulder) with higher amplitudes than *SKS* (left shoulder), which is not predicted by the PREM model. Because other traces at CCM do not show two distinct shoulders, site effects are ruled out; also, these anomalous effects are not seen for these three events at other stations (not shown), ruling out source mechanism effects.

[19] *SKS* and *SPdKS* are extremely close throughout the mantle, except where the P_{diff} segments occur in *SPdKS*; therefore the source of the anomalous waveforms is attributed to structure at the CMB, once source mechanism and site effects are ruled out (as discussed above). Similarly, highly anomalous records can be seen in Figure 4b near 112° for station WMQ; again, site effects can be ruled out. One of the anomalous WMQ records is observed in Figure 3d, where several records display anomalous waveforms. However, most records for that event have an impulsive *SKS* peak, suggesting that the anomaly observed at WMQ is likely attributable to CMB structure and not to source mechanism effects. The additional anomalous records seen in Figure 3d (CCM, FFC, SUR) also suggest anomalous CMB structure, somewhere along the P_{diff} paths.

3. Synthetic Seismograms

[20] A large bank of CMB boundary layer models (ULVZ, CRZ, CMTZ) were constructed for computation of synthetic seismograms to compare to our data, using the one-dimensional (1-D) reflectivity method [*Fuchs and Müller*, 1971; *Müller*, 1985]. *Helmberger et al.* [1996] found that the properties of 1-D synthetics were similar to those of 2-D synthetics. The main drawback in the 1-D approach is that boundary layer modeling cannot address structure confined to one side of the *SPdKS* path (i.e., the core entry versus exit location where P_{diff} occurs). Furthermore, using the 1-D approach, we cannot take into account focusing/defocusing effects of ULVZ or CMB topography, or volumetric heterogeneity, as can be modeled in two or three dimensions [e.g., *Wen and Helmberger*, 1998a]. Effects of D″ anisotropy are also excluded from modeling in the 1-D case; however, we do not expect this to affect our data. In addition, the reflectivity method makes use of the Earth flattening approximation, which may also affect the validity of large distance synthetic seismograms of core phases in the *P-SV* system [*Choy et al.*, 1980]. Nevertheless, as we are documenting relative changes in waveform behavior of *SPdKS* to *SKS*, we are still able to document the relative boundary layer anomalies responsible for the waveform changes by using the 1-D method. Furthermore, documentation of modeling trade-offs is straightforward, whereas this becomes increasingly difficult with 2-D or 3-D methods because of the increase in modeling degrees of freedom.

[21] In accordance with proposed models of boundary layer structure at the CMB, we created synthetic seismograms for CMTZ, CRZ, and ULVZ model spaces, using PREM as the reference model throughout the rest of the Earth. Synthetic seismograms were produced for a fine discretization in epicentral distance and source depth so every observation could be compared to predictions from every model. The types of models we used are summarized in Figure 5. We specifically explored variations in boundary

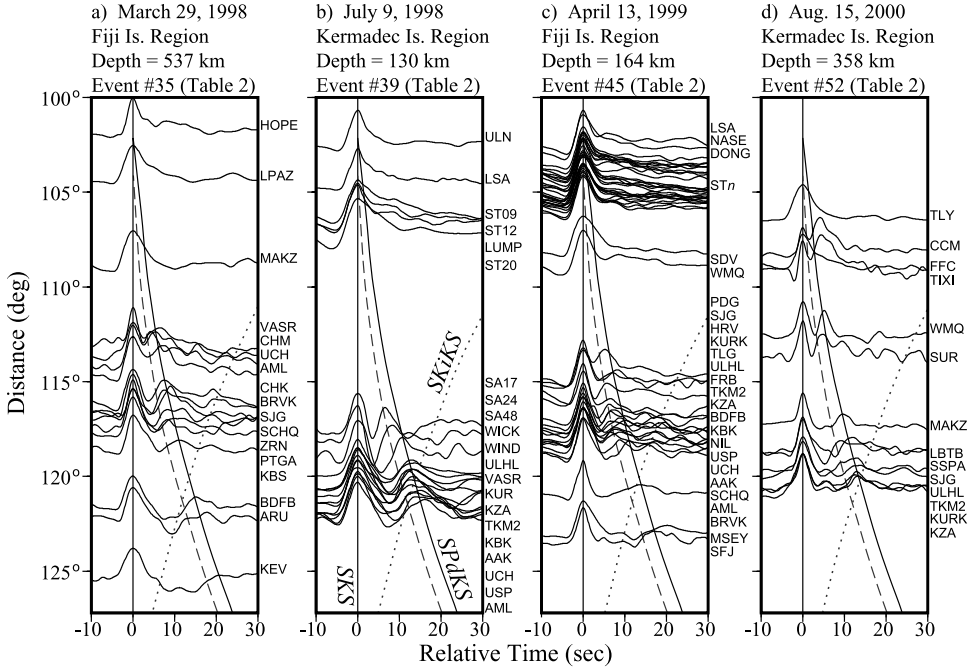

Figure 3. Distance profiles for four events. The radial component of displacement is shown. All records are normalized and centered on the *SKS* peak. The predicted *SPdKS* arrival is a dashed gray line for PREM and a solid black line for a ULVZ model (ULVZ model parameter values are $\delta V_P = -5\%$, $\delta V_S = -15\%$, $\delta\rho = +10\%$, thickness of 10 km). The dotted gray line shows the PREM prediction for the phase *SKiKS*. The recording station is shown to the right of each trace. STn in Figure 3c corresponds to 26 stations from the INDEPTH III PASSCAL experiment.

layer thickness (h, Figure 5), P and S wave velocity reductions, and density (ρ) increases; a summary of the ranges explored is given in Table 3. For ULVZ structures, two classes of models were considered: (1) an equal reduction of V_P and V_S (δV_P and δV_S, respectively), and (2) δV_S equal to 3 times δV_P. The first class of models is representative of a chemically distinct solid ULVZ, whereas the second corresponds to a partial melt origin of the ULVZ

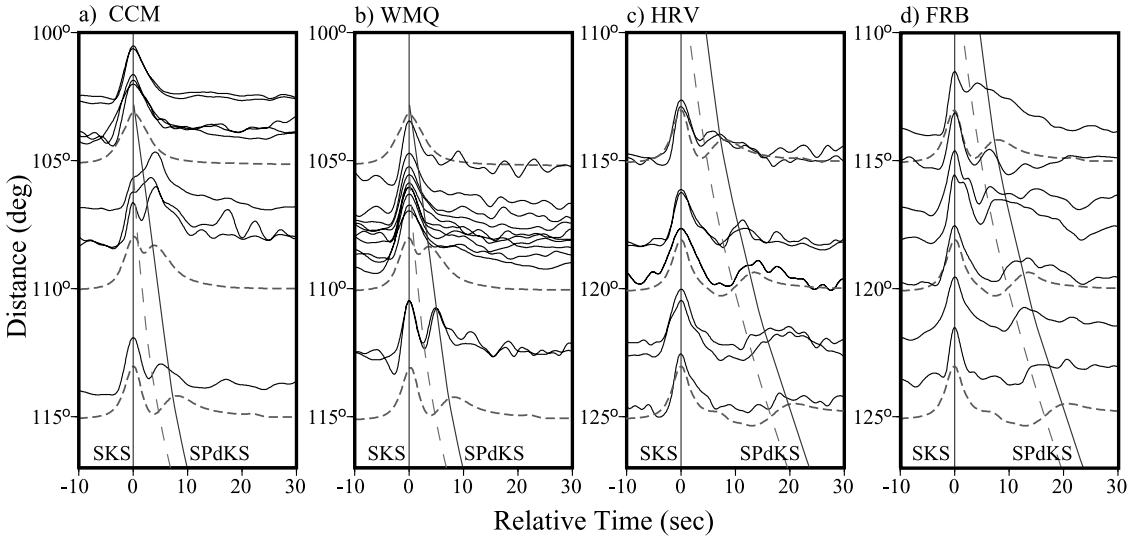

Figure 4. Radial component of displacement of four recording stations. All records are normalized and centered on the *SKS* peak. Each record is shifted in distance to accommodate varying source depth. The predicted arrival for *SPdKS* is shown for PREM (dashed gray line) and for a ULVZ model (solid black line; ULVZ model parameter values are $\delta V_P = -5\%$, $\delta V_S = -15\%$, $\delta\rho = +10\%$, thickness of 10 km). Also shown (dashed lines) are representative synthetic seismograms for this ULVZ model. Stations are (a) Cathedral Caves, Missouri; (b) Urumqi, Xinjiang, China; (c) Harvard, Massachusetts; and (d) Frobisher Bay, Canada.

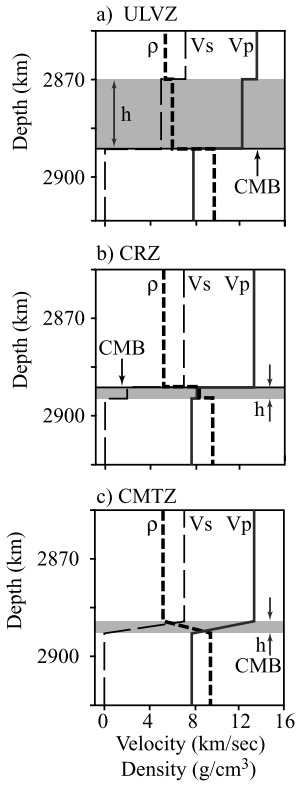

Figure 5. (a, b, and c) Velocity and density profiles with depth for ULVZ, CRZ, and CMTZ models, respectively. In Figures 5a and 5b, *h* represents the thickness over which mantle or core properties are modified for ULVZ or CRZ models. In Figure 5c, *h* represents the thickness over which the transition between mantle and core properties is modeled. Relevant parameters (compared to PREM on the mantle side) for models are, for Figure 5a, $\delta V_S = -30\%$, $\delta V_P = -10\%$, $\delta\rho = +10\%$, $h = 20$ km; for Figure 5b, $\delta V_S = -72\%$, $\delta V_P = -38\%$, $\delta\rho = +60\%$, $h = 3$ km; and for Figure 5c, $h = 3$ km.

[*Williams and Garnero*, 1996]. For both cases, δV_P, δV_S, ρ, and ULVZ thickness were allowed to vary (Figure 5a). We created CRZ models by assuming there is a small finite rigidity at the top of the core. To accommodate this assumption, CRZ models were created by assuming a nonzero value of *S* wave velocity (V_S) in the outer core, and rigidity (μ) calculated from $\mu = \rho V_S^2$. This nonzero rigidity perturbs the outermost core *P* wave velocity ($V_P = [(K + 4/3\mu)/\rho]^{1/2}$) in the CRZ, making it larger than that of PREM (by up to 33%). Hence, with CRZ models we allowed thickness, density, and V_S to vary, which involve V_P perturbations due to finite μ (Figure 5b). CMTZ models were created with a linear gradient from lower mantle properties at the top of the CMTZ layer to outer core properties at the bottom of the CMTZ layer. CMTZ models are centered in depth on the CMB with layer thickness as the only variable (Figure 5c).

[22] The parameter range for each model space (Table 3) was discretized as follows: for both classes of ULVZ models, ULVZ thickness was modeled as being 2, 5, 10, or 30 km, and lowermost mantle ρ was modeled as a 0, 10, 20, 40, or 60% increase (i.e., relative to the PREM mantle). For class 1, equal δV_P and δV_S reductions ranged from 0, 5, 10, 15, 20, to 30%. For class 2, δV_P and δV_S reductions of 5 and 15%, 10 and 30%, 15 and 45%, or 20 and 60%, respectively (i.e., $\delta V_S = 3\delta V_P$), were tested. This resulted in 200 unique ULVZ models. CRZ models were discretized in 1.0 km thickness increments, resulting in four unique CRZ thicknesses. Additionally, the CRZ layer contained nonzero V_S between 1.0 and 5.0 km/s in 1.0 km/s increments and outer core density reductions by up to -50% in 10% increments. Therefore our CRZ model space consisted of 4 thicknesses $\times$ 5 V_S values $\times$ 6 ρ reductions, equaling 120 distinct CRZ models. For CMTZ models, thickness (the only variable) was discretized in 0.25 km increments, resulting in 11 unique models. Thus our model space consisted of synthetic seismograms for 333 distinct models that span the range of parameters in Table 3. Synthetic seismogram construction for each model for a range of source depths and distances resulted in nearly 200,000 synthetic seismograms in our model space database to be compared to data traces.

[23] Previous modeling of ULVZ structure has shown evidence for low-quality factor (Q) values [*Havens and Revenaugh*, 2001], which may be expected if the ULVZ structure is composed of partial melt. However, in creating this synthetic model space we do not consider variations in Q. This is primarily an effort to limit the number of parameters, noting that extremely low Q (e.g., $Q\mu = 5$, $Q_K = 5$) variations will lower *SPdKS* amplitudes but roughly retain relative *SKS-SPdKS* timing [*Garnero and Helmberger*, 1998]. Nevertheless, future efforts should consider Q, especially for probes that demonstrate a first-order sensitivity to it.

4. Modeling Approach

[24] In order to compare *SPdKS* observations to synthetic predictions we first constructed an empirical source for each of the events used in this study (Table 2). On an event-by-event basis, *SKS* pulses were stacked if (1) they were at pre-*SPdKS* distances between 90° and 100°; (2) they were clean and impulsive; and (3) they had a high degree of waveform

Table 3. Synthetic Model Space Parameter Ranges[a]

Model	min V_S, km/s	max V_S, km/s	min V_P, km/s	max V_P, km/s	min ρ, g/cm^3	max ρ, g/cm^3	Thickness, km
ULVZ[b]	5.08 (−30)	7.26 (0)	9.60 (−30)	13.72 (0)	5.57 (0)	8.91 (60)	2.0–30.0
ULVZ[c]	2.91 (−60)	6.17 (−15)	10.97 (−20)	13.03 (−5)	5.57 (0)	8.91 (60)	2.0–30.0
CRZ	1.00 (−86)	5.00 (−31)	8.20 (−40)	10.70 (−22)	4.95 (−11)	9.90 (77)	0.5–3.5
CMTZ	NA	NA	NA	NA	NA	NA	0.5–3.0

[a]Percentages (values in parentheses) are referenced to properties on the mantle side of the CMB relative to PREM. NA indicates not applicable.
[b]ULVZ models with $\delta \ln V_S = \delta \ln V_P$.
[c]ULVZ models with $\delta \ln V_S = 3*\delta \ln V_P$.

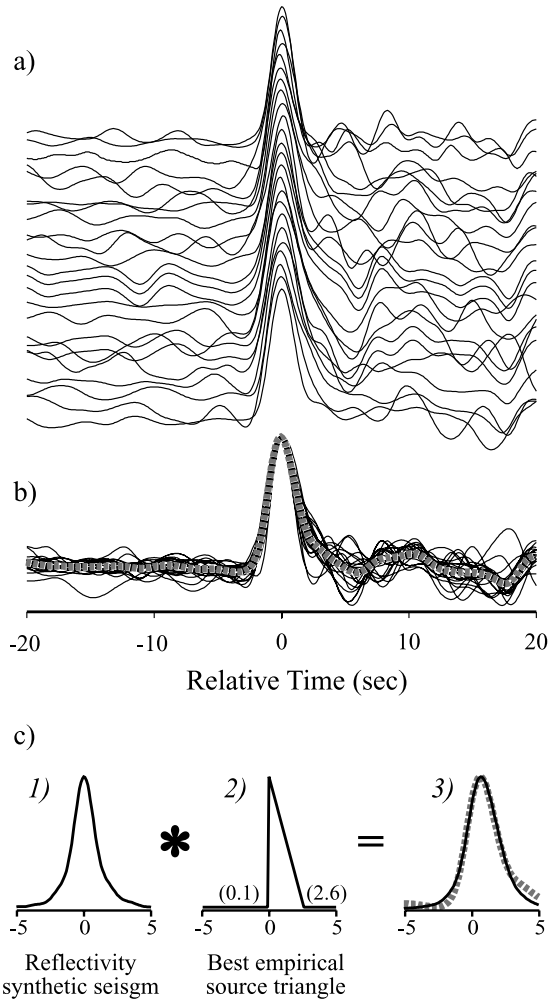

Figure 6. Empirical source modeling. (a) Twenty-four records windowed, centered, and normalized on the *SKS* peak for the 14 April 1998 Fiji Islands event (event 37, Table 2). The traces are all records accepted for stacking with a cross-correlation coefficient of at least 0.85, in the distance range of 92°–98°. (b) Individual traces overlain, with the dashed gray line indicating the resulting stack. (c) Method of determining the empirical source, by (left) taking the synthetic seismogram centered on *SKS* at 95° epicentral distance and (middle) convolving the synthetic with a triangle or truncated triangle function (in this case, a triangle function with width 0.1 s to the left of zero and 2.6 s to the right of zero) that best fits the stacked data (dashed gray line) shown on the right.

similarity, manifest in a high cross-correlation (CC) coefficient with other records for that event. Figure 6 shows an example empirical source construction, where 24 individual *SKS* records between 90° and 100° (Figure 6a) are summed (Figure 6b) for event 30 (Table 2). The dashed gray line is the resulting linear stack and is shown overlain on the original 24 traces. For each event the following steps were carried out to best incorporate the empirical source in our synthetic modeling:

[25] 1. We conducted a systematic grid search for a triangle function that when convolved with a pre-*SPdKS* distance PREM synthetic seismogram returned the best CC coefficient with our empirical source function (Figure 6c, step 3). We created triangle functions by starting with a delta function and then alternately varying the right- and left-hand width of the triangle in 0.1 s increments, which included both symmetric and asymmetric triangle functions. Truncated triangle functions were also considered.

[26] 2. The best fitting triangle function was convolved with all synthetic seismograms in our model space.

[27] 3. A 45 s time window containing *SKS* and *SPdKS* for all data and synthetics (at appropriate source depths and distances) was constructed. Each data record was cross-correlated with the appropriate depth and distance synthetic seismogram of all of the 333 models. The resulting CC coefficient was stored for all possible combinations, and visual inspection of results was also made from graphical overlays of all data-model comparisons.

[28] *SKS* waveforms used for empirical source construction (recorded between 90° and 100°) intersect the CMB at a supercritical angle resulting in a small phase shift, thus introducing a slight shoulder in our waveforms (observable on individual traces in Figure 6). For distances greater than that for *SPdKS* inception this phase shift disappears. This does not strongly affect our source construction, as the width of the central *SKS* peak is well fit by our model. However, the shoulder introduces a slight asymmetry of our triangle functions to the right-hand side. Where the asymmetry became too large, we shortened the window over which we calculated the CC coefficient so as to not include the shoulder, thus retaining symmetric empirical source functions.

[29] We grouped records into four basic categories on the basis of data-synthetic CC coefficients.

[30] 1. For PREM waveforms, the observation-PREM synthetic CC coefficient ranked higher than all other data-synthetic combinations (we note that the use of the term "PREM" here and hereafter is simply meant to signify the lack of any significant low-velocity boundary layering at the CMB, the 1-D reference model is unimportant).

[31] 2. For probable low-velocity zone (PLVZ) waveforms, the highest data-synthetic CC coefficients correspond to synthetic models having very thin boundary layers (typically <5 km in thickness) but do not differ significantly from the PREM CC coefficient. We chose a relative percent difference of CC coefficients of 5% as our cutoff. That is, if the CC coefficient of the PREM model was within 5% of the CC coefficient of the best fitting model, the record was classified as PLVZ.

[32] 3. For the boundary layer structure (ULVZ) waveforms, the highest data-synthetic CC coefficients are from significant CMB boundary layer model synthetics (hereafter we refer to these waveforms as simply "ULVZ," although CRZ, or CMTZ models may apply as well). For this case, the PREM CC coefficient normalized to that of the best fitting model is below 95%.

[33] 4. For extreme waveforms, observations are not adequately fit by any synthetic in our model space; typically, these waveforms exhibited much higher amplitudes of *SPdKS* relative to *SKS* (as seen in Figure 4a, 108°) than are present in any of our models. In some cases this may be indicative of 2- or 3-D structure causing focusing effects; however, further investigation is needed in order to explain these records. Records of this class are assumed to sample

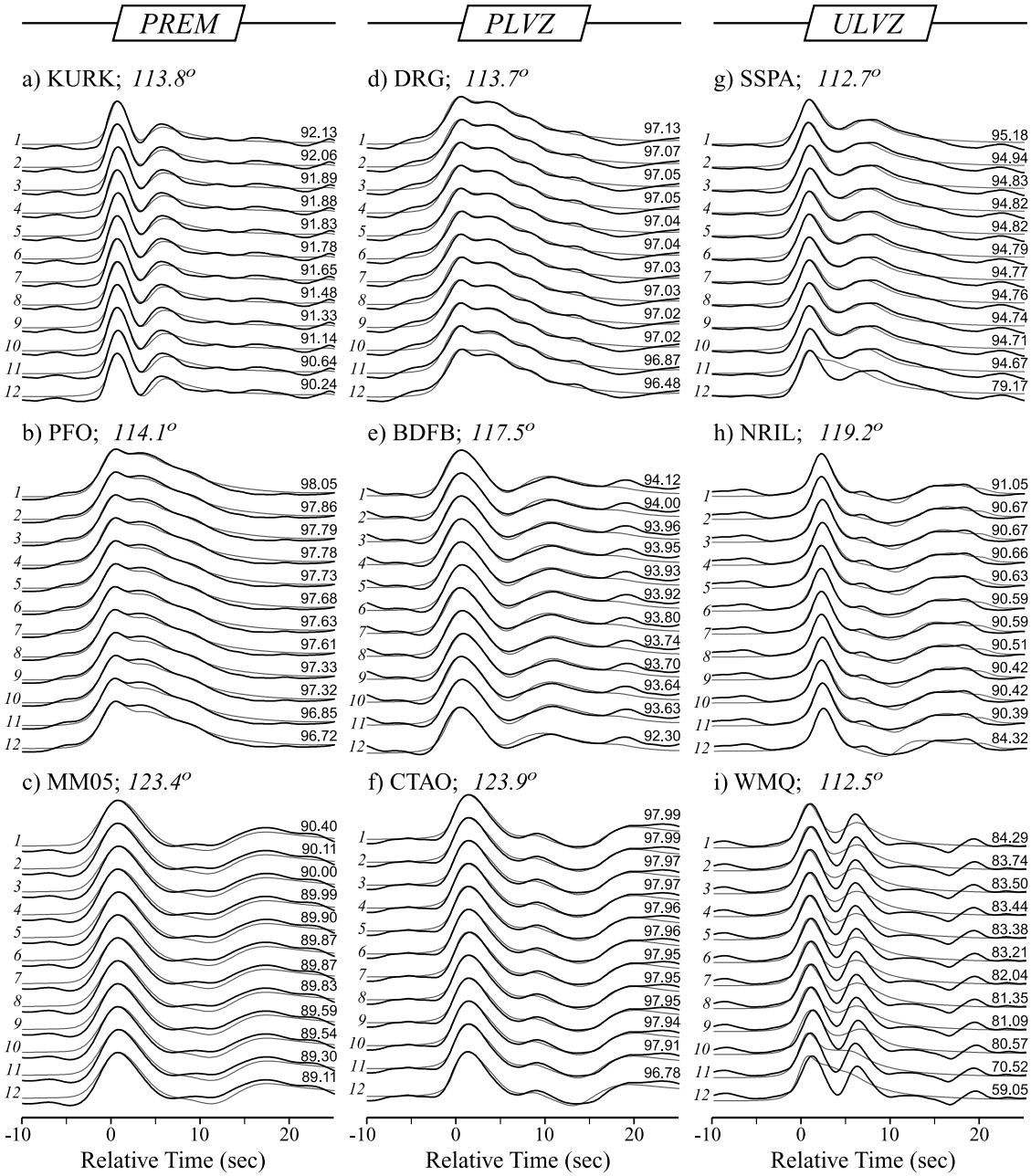

Figure 7. Cross correlation of records with model synthetics. (a, b, and c) Records classified as PREM; (d, e, and f) example records classified as PLVZ; (g and h) records classified as ULVZ; and (i) an example of a record classified as ELVZ. The dark line is data, repeated through each panel compared to the light colored line of the synthetics. Epicentral distances and station names for each record section are shown above the traces. Just above each data/model overlay on the right is the CCC of the record compared to the model synthetic. Model details are given in Table 4 (numbers to the left of each trace correspond with Table 4). Events used to make this figure are for those listed in Table 2 for the following dates: KURK, 18 December 2000; PFO, 25 December 1995; MMO5, 14 August 1995; DGR, 25 December 1995; BDFB, 13 April 1999; CTAO, 10 May 1994; SSPA, 16 May 1998; NRIL, 21 March 1997; WMQ, 15 August 2000.

an extreme low-velocity zone, or ELVZ. No CC coefficient-based modeling for ELVZ waveforms is made because of the high degree of variability of these records (and subsequent CC coefficients). The lack of a well-defined basis for classification of ELVZ records does not produce problems in our analyses, as we only use the ELVZ characterization in searching for spatial groupings of P_{diff} segments that display similar properties and may elucidate highly anomalous regions of the CMB.

[34] Figure 7 shows examples of comparisons between data (bold lines) and synthetics (thin lines). Figures 7a–7c present observed waveforms best fit by the PREM model. Observation-prediction comparisons are shown for PREM along with 11 models having the next highest cross-

Table 4. Model Parameters Corresponding to Figure 7

	KURK, 113.8°						DRG, 113.7°						SSPA, 112.7°					
	CCC, %	Model	$-V_S$,%	$-V_P$,%	+ρ,%	h, km	CCC, %	Model	$-V_S$,%	$-V_P$,%	+ρ,%	h, km	CCC, %	Model	$-V_S$,%	$-V_P$,%	+ρ,%	h, km
1	92.13	PREM	-	-	-	-	97.13	CRZ	86	40	7	0.5	95.18	ULVZ	15	5	40	5
2	92.06	CRZ	31	22	−11	0.5	97.07	CRZ	72	38	24	0.5	94.94	ULVZ	5	5	20	10
3	91.89	ULVZ	5	5	0	2	97.05	CRZ	45	28	42	0.5	94.83	ULVZ	20	20	0	5
4	91.88	CRZ	45	28	−11	0.5	97.05	ULVZ	15	5	10	2	94.82	CRZ	31	22	42	2.5
5	91.83	CRZ	59	34	−11	0.5	97.04	CRZ	31	22	60	0.5	94.82	ULVZ	45	15	40	2
6	91.78	CRZ	72	38	−11	0.5	97.04	ULVZ	10	10	10	2	94.79	CRZ	45	28	60	1.5
7	91.65	CMTZ	-	-	-	0.25	97.03	ULVZ	5	5	0	5	94.77	ULVZ	15	15	10	5
8	91.48	CRZ	86	40	−11	0.5	97.03	CMTZ	-	-	-	0.5	94.76	ULVZ	30	10	60	2
9	91.33	ULVZ	10	10	0	2	97.02	ULVZ	15	15	0	2	94.74	CRZ	59	34	42	1.5
10	91.14	ULVZ	15	5	0	2	97.02	CRZ	59	34	42	0.5	94.71	CMTZ	-	-	-	1.75
11	90.64	CMTZ	-	-	-	0.5	96.87	ULVZ	20	20	0	2	94.67	ULVZ	60	20	20	2
12	90.24	ULVZ	15	15	0	2	96.48	PREM	-	-	-	-	79.17	PREM	-	-	-	-
	PFO, 114.1°						BDFB, 117.5°						NRIL, 119.2°					
	CCC, %	Model	$-V_S$,%	$-V_P$,%	+ρ,%	h, km	CCC, %	Model	$-V_S$,%	$-V_P$,%	+ρ,%	h, km	CCC, %	Model	$-V_S$,%	$-V_P$,%	+ρ,%	h, km
1	98.05	PREM	-	-	-	-	94.12	ULVZ	30	10	10	2	91.05	ULVZ	30	30	60	2
2	97.86	CRZ	31	22	−11	0.5	94.00	CRZ	86	40	78	0.5	90.67	ULVZ	15	15	20	5
3	97.79	ULVZ	5	5	0	2	93.96	ULVZ	45	15	10	2	90.67	ULVZ	10	10	40	5
4	97.78	CRZ	48	28	−11	0.5	93.95	ULVZ	10	10	60	2	90.66	CRZ	45	28	78	1.5
5	97.73	CRZ	59	34	−11	0.5	93.93	CMTZ	-	-	-	1.25	90.63	ULVZ	20	20	10	5
6	97.68	CRZ	72	38	−11	0.5	93.92	ULVZ	15	5	10	5	90.59	ULVZ	5	5	40	10
7	97.63	CMTZ	-	-	-	0.25	93.80	ULVZ	5	5	0	10	90.59	ULVZ	5	5	20	10
8	97.61	CRZ	86	40	−11	0.5	93.74	ULVZ	60	20	0	2	90.51	ULVZ	30	30	40	2
9	97.33	ULVZ	10	10	0	2	93.70	CRZ	72	38	7	1.5	90.42	ULVZ	10	10	60	5
10	97.32	ULVZ	15	5	0	2	93.64	ULVZ	20	20	40	2	90.42	CRZ	31	22	42	1.5
11	96.85	CMTZ	-	-	-	0.5	93.63	CRZ	59	34	24	1.5	90.39	CRZ	45	28	60	2
12	96.72	ULVZ	15	15	0	2	92.30	PREM	-	-	-	-	84.32	PREM	-	-	-	-
	MM05, 123.4°						CTAO, 123.9°						WMQ, 112.5°					
	CCC, %	Model	$-V_S$,%	$-V_P$,%	+ρ,%	h, km	CCC, %	Model	$-V_S$,%	$-V_P$,%	+ρ,%	h, km	CCC, %	Model	$-V_S$,%	$-V_P$,%	+ρ,%	h, km
1	90.40	PREM	-	-	-	-	97.99	CRZ	86	40	78	0.5	84.29	ULVZ	20	20	60	2
2	90.11	CRZ	31	22	−11	0.5	97.99	CRZ	59	34	7	1.5	83.74	ULVZ	30	30	20	2
3	90.00	ULVZ	5	5	0	2	97.97	ULVZ	15	15	40	2	83.50	ULVZ	10	10	20	5
4	89.99	CRZ	45	28	−11	0.5	97.97	CMTZ	-	-	-	1	83.44	ULVZ	5	5	60	5
5	89.90	CRZ	59	34	−11	0.5	97.96	ULVZ	10	10	10	5	83.38	ULVZ	15	15	0	5
6	89.87	CMTZ	-	-	-	0.25	97.96	CRZ	31	22	42	1.5	83.21	CRZ	31	22	60	1.5
7	89.87	CRZ	72	38	−11	0.5	97.95	ULVZ	20	20	40	2	82.04	ULVZ	30	10	40	2
8	89.83	CRZ	86	40	−11	0.5	97.95	ULVZ	30	30	10	2	81.35	ULVZ	15	5	20	5
9	89.59	ULVZ	10	10	0	2	97.95	ULVZ	45	15	0	2	81.09	ULVZ	45	15	10	2
10	89.54	ULVZ	15	5	0	2	97.94	ULVZ	30	10	20	2	80.57	ULVZ	60	20	0	2
11	89.30	CMTZ	-	-	-	0.5	97.91	CRZ	72	38	78	0.5	70.52	CMTZ	-	-	-	0.5
12	89.11	ULVZ	15	15	0	2	96.78	PREM	-	-	-	-	59.05	PREM	-	-	-	-

correlation coefficient. Cross-correlation coefficients are displayed to the right of each overlay, and model properties are listed in Table 4. Because of the fine discretization of the model space (i.e., models span properties that are only slight perturbations from PREM, up to more extreme ULVZ structures), only a gradual degradation in fit from the best fit PREM prediction is seen. Nonetheless, PREM is the best fit. For example, Figure 7a shows that slight CMB perturbations result in *SPdKS* delays relative to *SKS*, which degrades the CC goodness of fit. Figures 7d–7f show examples of the PLVZ observations and predictions. The 11 best fitting synthetics are overlain on the data, and the twelfth overlay is the data and PREM. All waveform complexities are better reproduced by models with a thin anomalous boundary layer, though the PREM fit only slightly differs from the fits with higher cross-correlation coefficients. For example, the best fit normalized CC coefficient for PREM for Figure 7d is $100 \times (1-96.48/97.13)$ or ∼0.7%; these data are thus grouped into the PLVZ category. Figures 7g and 7h show data and synthetic comparisons for the boundary layer structure category (ULVZ). The data are fit by significant (>5% relative difference in CC coefficients) low-velocity CMB layering (contrast with the PREM synthetic at the bottom of each panel); and Figure 7i displays a comparison for the ELVZ waveform category. This record could not be explained adequately by any of our models constructed and was thus grouped into the extreme category.

[35] It is noteworthy that the model giving the highest cross-correlation coefficient does not necessarily fit the observation the best in terms of *SPdKS* amplitude and timing. For example, in Figure 7e for station BDFB (Brasilia, Brazil), *SPdKS* is observed to arrive slightly later than predicted by the model with the highest CC coefficient. This *SPdKS* arrival time may be better predicted by one of the models with a lower ranking cross-correlation coefficient; however, the downswing between *SKS* and *SPdKS* is over-predicted. Furthermore, notable model parameter trade-offs

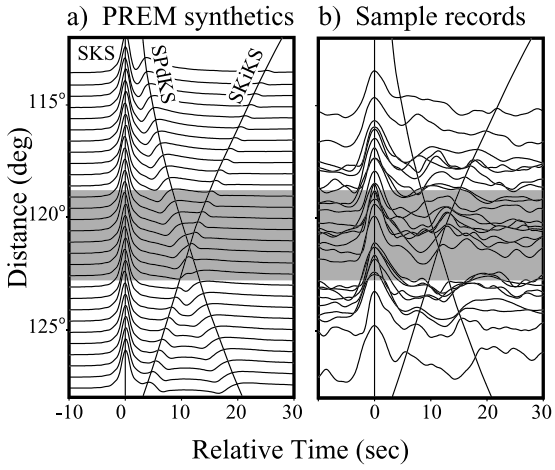

Figure 8. (a) Sample PREM synthetic seismograms centered and normalized on *SKS* for a 400 km deep event. Black lines show predicted arrivals for *SPdKS* and *SKiKS*. *SKiKS* is observed to interfere with *SPdKS* waveforms in the dark shaded region. (b) Twenty-six records from varying events centered on *SKS* and shifted to a common source depth of 400 km.

can be seen between models ranked nearly the same in CC coefficient. These 1-D model trade-offs between thickness, density, and velocity variations have been explored in previous work [*Garnero and Helmberger*, 1998; *Garnero and Jeanloz*, 2000a] and show the difficulty in uniquely constraining model parameters. Thus determination of the best model parameters describing an individual record is difficult and potentially subject to personal bias. This is a primary motivation for grouping our observations into the previously described four categories. We note that the CC method is both useful, in that it aids in large data set processing, and has shortcomings, given that important waveform subtleties are difficult to address.

[36] In modeling *SPdKS* observations, additional considerations must also be taken into account. First, *SPdKS* waveforms may undergo constructive and destructive interference with the phase *SKiKS* that is observable in broadband data. Figure 8 shows PREM synthetics and sample records that may exhibit interference from *SKiKS*. The shaded distance range shows the region of maximum potential interference of *SKiKS* as predicted by PREM for an event with a 400 km source depth. The distance range represented by this gray box can shift to greater distances (by 1°–2°) with the presence of low-velocity CMB structure. Several traces seem to be affected by this interference as evidenced by broadened *SPdKS* arrivals (e.g., near 120° in Figure 8b). This interference further complicates the waveform modeling and must be considered in modeling of broadband *SPdKS* waveforms as in this study.

[37] Finally, the uniqueness of model fit is highly dependent on epicentral distance. Records from the *SPdKS* inception distance up to ~112° contain the most diagnostic waveshape distortions due to *SPdKS* modulating the peak, shoulder, and downswing of *SKS*. Larger distance recordings are more difficult to uniquely constrain, as *SPdKS* is a longer-period pulse that has sampled a much longer path along the CMB, as well as structure above the CMB. These records, even in regions known to contain strong CMB anomalies, often appear PREM-like. This can be observed in Figure 7f for station CTAO (Charters Towers, Australia) at 123.9°; models with large ULVZ characteristics do not remarkably vary from PREM (<5% CC coefficient difference), whereas for station SSPA (Standing Stone, Pennsylvania) at 112.7° (Figure 7g) the boundary layer models show characteristics of waveshape distortions that are quite distinguishable from PREM (>5% CC coefficient difference).

[38] The dependency of uniqueness of fit on epicentral distance is further explored in Figure 9. Most of the *SPdKS* distance range studied here is densely sampled (Figure 9a). The CC coefficient between each observation and PREM was divided by the cross-correlation coefficient of the best fitting synthetic for that record. This normalized PREM data CC coefficient is averaged in 2.5° distance bins and shown in Figure 9b. The error bars represent 1 standard deviation of the mean. In Figure 9b a value of 1 represents the best fit synthetic and PREM being indistinguishable. The bins between 105° and 110° are close to PREM as for most of the global data, *SPdKS* anomalies are typically not yet manifested as *SKS* waveform distortions. Between 110° and 115°, however, these distortions are easily viewed and start to degrade the CC coefficient between data and PREM.

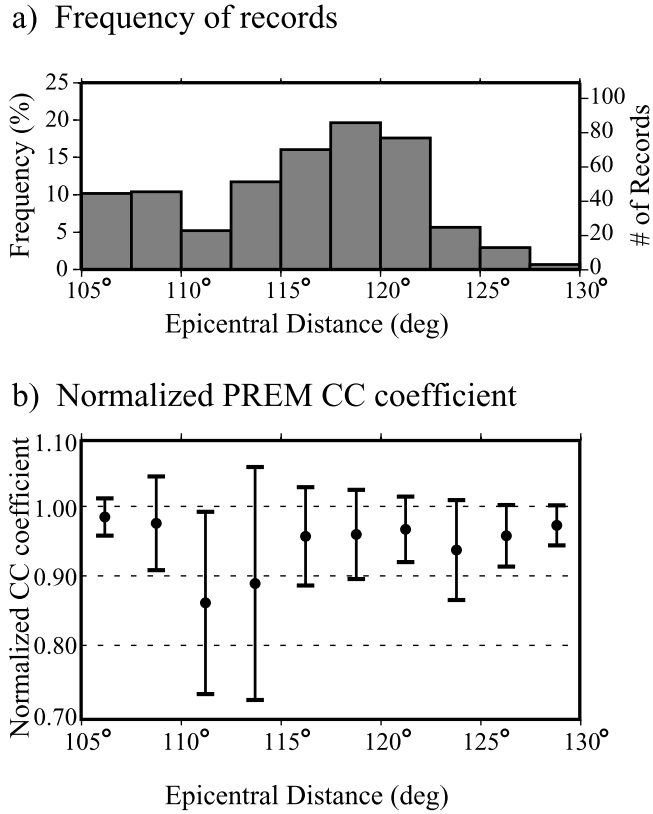

Figure 9. (a) Amount of records used in this study grouped into 2.5° epicentral distance bins. (b) Average and 1 standard deviation of all normalized cross-correlation coefficients grouped in the same distance bins as in Figure 9a. The normalized cross-correlation coefficient is cross-correlation coefficient for a PREM synthetic compared to a record/cross-correlation coefficient for the synthetic of the best fitting model for a record.

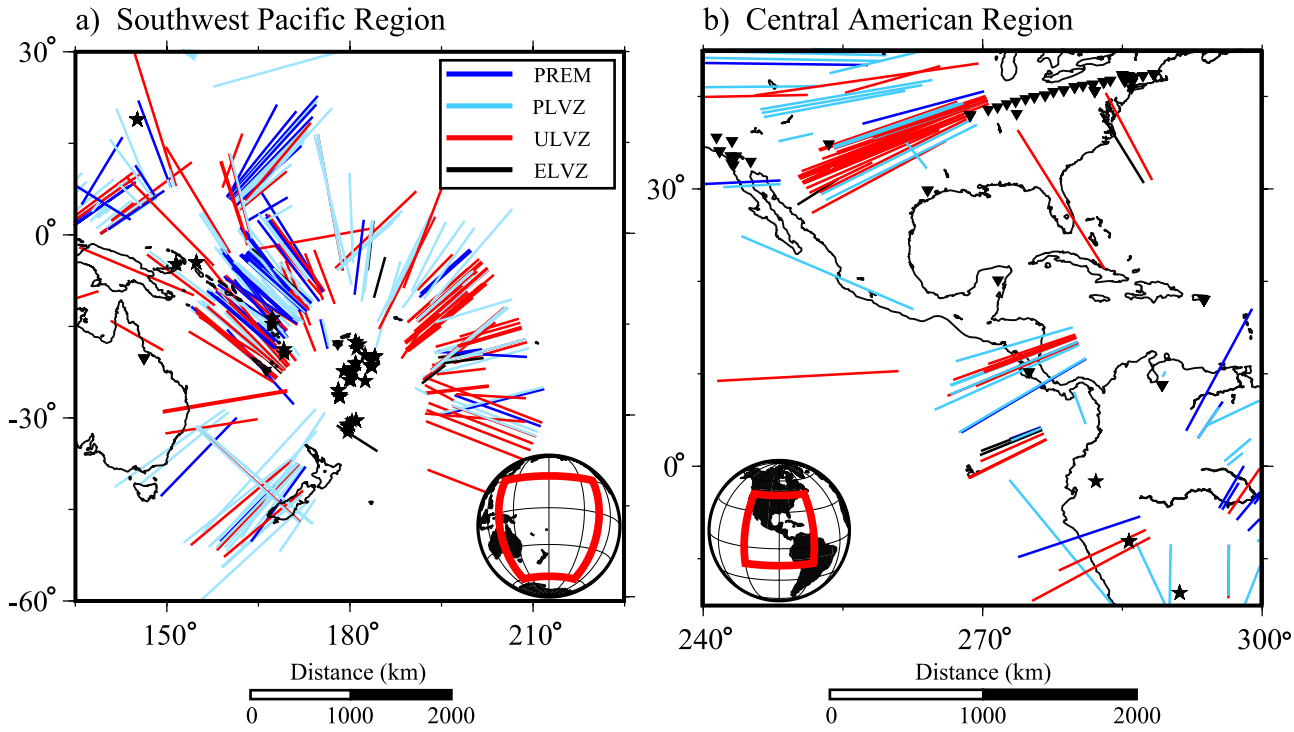

Figure 10. Regional maps centered in the (a) southwest Pacific and (b) Central America regions. Lines represent the P_{diff} segments of *SPdKS* on the CMB. Dark blue lines represent paths for which the waveforms behaved as PREM. Light blue lines represent paths that are characterized as PLVZ. Red lines are used for waveforms that are characterized as ULVZ, and black lines represent ELVZ waveforms. Stars indicate event locations, and triangles represent station locations. The distance scale beneath each panel is the distance at the equator on the CMB.

The large increase in the standard deviation indicates the ability to better distinguish between models for this distance range. At larger distances, both the timing and amplitude of *SPdKS* do not differ that remarkably from PREM, resulting in the average normalized CC coefficient again approaching the PREM value (thus indicating the reduction in ability of the data beyond 115° to strongly constrain CMB boundary layer structure).

5. Inferred ULVZ Distribution

5.1. Quantifying ULVZ Strength and Trade-offs

[39] Our synthetic seismogram model space spans three classes of models: ULVZ, CRZ, and CMTZ (Figure 5). Each record (of collected data) was compared to synthetics of every model in each of these model classes. As mentioned previously (section 4), there are strong modeling trade-offs between the different model types, particularly for the larger distance data. Also, only relatively subtle changes exist between associated CC coefficients between data and best fit ULVZ, CRZ, or CMTZ synthetics for the larger distances. This often precludes constraining whether any particular model class best explains a given record. Nonetheless, it is still possible to characterize how anomalous data are in a relative sense by looking at geographical trends in data best fit by PREM (i.e., normal mantle), probable low-velocity zones (PLVZ), or anomalous boundary layer structure (ULVZ), where we use "ULVZ" to represent moderate ULVZ, CRZ, or CMTZ. We have thus classified best fitting models of each observation in this fashion: (1) PREM, (2) PLVZ, (3) ULVZ, and (4) ELVZ. Although we are not able to determine specific boundary layer properties (e.g., layer thickness, density, and velocity perturbation) because of trade-offs, we infer structure in terms of relative waveform behavior by the four listed categories.

[40] By looking at the distribution of *SPdKS* P_{diff} segments on the CMB, we are able to observe the geographical distribution of waveform behavior for individual records. Figure 10 shows two regions of the CMB (the same regions presented in Figure 1) with P_{diff} segments color-coded on the basis of our waveform behavior classification scheme. Several P_{diff} segments best modeled as having ULVZ-like structure are in close proximity to P_{diff} segments best modeled as exhibiting PREM-like structure. A high degree of lateral heterogeneity is observed, where in some cases the P_{diff} CMB entry point for ULVZ- and PREM-type waveforms is only on the order of tens of kilometers apart. Lateral heterogeneity at such short-scale lengths has been observed in previous studies [*Garnero and Helmberger*, 1996; *Rost and Revenaugh*, 2001; *Wen*, 2001; *Rost and Revenaugh*, 2003] and is consistent with a CMB environment of high variability and complexity.

[41] Despite the close proximity of P_{diff} segments grouped into PREM or ULVZ categories, to first order, there exist localized groupings of similarly characterized P_{diff} segments. For example, Figure 10a shows that east of the Tonga and Kermadec Trenches, the majority of P_{diff} segments are characterized as ULVZ; to the south most

segments are characterized as PLVZ. To the west (at $\sim -15^\circ$ latitude), there exists a tight grouping of segments classified as ULVZ that transitions into PREM and PLVZ to north and northwest. The predominance of P_{diff} segments (on the source side) characterized as ULVZ to the west of the Tonga and Kermadec Trenches are also manifested in a close grouping of ULVZ classified segments (on the receiver side) under central North America ($\sim 30^\circ$ latitude; Figure 10b). However, without crossing coverage we are unable to determine if an ULVZ exists under the southwest Pacific, North America, or both regions.

5.2. ULVZ Likelihood Maps

[42] Even in the presence of extremely short-scale heterogeneity, it is useful to address the intermediate- to long-wavelength geographical distribution of ULVZ heterogeneity. Here we describe an averaging scheme that maps the likelihood of any part of the CMB sampled by our data being best characterized with or without anomalous low-velocity boundary layering. For this purpose we have divided the CMB into $5^\circ \times 5^\circ$ cells. To best quantify ULVZ existence/nonexistence, the number of *SPdKS* P_{diff} segments that pass through each grid cell have been tabulated and assigned "*SPdKS* values" as follows: PREM-like *SPdKS* segments have been assigned a value of 0.0 (thus zero "ULVZ likelihood"), PLVZ-like segments have also been assigned a value of 0.0, ULVZ-like segments have been assigned a value of 1.0 (i.e., maximum ULVZ likelihood), and ELVZ-like segments have also been assigned a value of 1.0 (where waveforms with extreme *SPdKS* anomalies are assumed to be due to boundary layer structure). This enables a cell-by-cell average that permits assessment of solution structure uniformity, as well as geographical ULVZ distribution.

[43] We define the ULVZ likelihood for each sampled cell by averaging all *SPdKS* values in each cell. That is, we sum the "*SPdKS* value" of all P_{diff} segments on the basis of PREM predicted ray paths, passing through one of our $5^\circ \times 5^\circ$ cells, and weight the sum by the total number of rays that passed through the cell. If all *SPdKS* P_{diff} segments passing through a given cell were classified as ULVZ-like, then its ULVZ likelihood would correspond to 1.0. If all data were classified as PREM-like, its ULVZ likelihood would correspond to 0.0. Figure 11 shows the resulting ULVZ likelihood for our *SPdKS* data set. Figure 11a shows our entire data set with PREM predicted source- and receiver-side P_{diff} segments colored red and blue, respectively. In section 4 we noted that records in the epicentral distance range between 110° and 115° provide the greatest uniqueness of fit (Figure 9). For longer source-receiver distances the uniqueness of fit degrades. Figure 11b shows our data coverage for each $5^\circ \times 5^\circ$ cell for our most distinctive data (restricted between 110° and 120°), where we have colored each grid cell by the number of P_{diff} segments passing through a cell, and Figure 11c shows the ULVZ likelihood for this restricted range.

[44] When comparing this ULVZ likelihood map (Figure 11c) with a comparable likelihood map utilizing all data (available in the auxiliary material[1]), the two ULVZ likelihood maps critically depend on how uniquely *SKS-SPdKS* waveform characteristics can reveal CMB structure. While both maps agree with each other to first-order at long wavelength, distinct differences exist for some regions. Restricting the distance range has enhanced ULVZ likelihood in many regions by discarding the longest-distance (poorly constrained) PREM fit data. We consider the first map (Figure 11c) to be the more constrained estimation of ULVZ likelihood.

[45] The ULVZ likelihood maps reveal regional-scale ULVZ patterns. For example, the southwest Pacific region and Central America region show high ULVZ likelihood. Strong ULVZ likelihood is observed under the Indian Ocean, although we do not have complete coverage here. On the other hand, the central east Asia region is extremely well sampled and shows no ULVZ likelihood. The central and eastern African CMB region also shows lesser likelihood of ULVZ, although we note that this is not well sampled. The area beneath (and west of) Kamchatka displays evidence for ULVZ existence, which is a region where no ULVZ has previously been observed. Other regions, such as the area east of the Philippines, are dominated by moderate to low ULVZ likelihood (midway between ULVZ and PREM). These regions likely contain a high degree of heterogeneity as suggested by the multiple P_{diff} segments of varying classifications passing through each cell (also see Figure 10).

[46] Many studies have focused on the southwest Pacific and Central America regions (Figure 1 and Table 1). The southwest Pacific region has displayed compelling evidence for ULVZs utilizing varied approaches. To the west and northwest of the Tonga and Kermadec Trenches, short-scale length heterogeneity has been argued in studies utilizing short-period precursors to the phase *ScP* (studies 5, 7, 10, and 11 in Table 1 and Figure 1). These studies show *ScP* bounce points located within tens of kilometers on the CMB displaying waveforms indicative of both existence and nonexistence of ULVZ structure. Our study also shows this high degree of lateral heterogeneity in these regions, with ULVZ likelihood in the range of 0.5–0.8 (Figure 11c). Studies focusing west of the Tonga and Kermadec Trenches have agreed on positive ULVZ sighting. This region also contains some of our highest ULVZ likelihood values. Yet, we also observe intermingled PREM- and PLVZ-like waveforms, suggesting that this region is more complicated than previously suggested. A variety of results have emerged from studies looking at the Central America region. Nearly all of our data for this region display either ULVZ or PLVZ-like waveforms. Of special note is the tight grouping of ULVZ- and ELVZ-like waveforms just to the east of the Galapagos Islands, supporting the findings of studies 4 and 18 (Table 1 and Figure 1).

[47] Several studies have searched for ULVZ structures in regions not encompassed in Figure 1. The northeast Pacific region has received much attention from studies of short-period precursors to core reflected phases (see Table 1), although the majority of these studies have not shown any evidence of ULVZ structure. Our likelihood map is in agreement with no ULVZ under the northeast Pacific; however, we only sparsely sample this region. *Wen* [2001] studied the southern Indian Ocean using travel times and waveform analysis of *S*, *ScS*, SH_{diff}, and P_{diff} from four events and found a trend of PREM-like lowermost mantle in

[1] Auxiliary material is available at ftp://ftp.agu.org/apend/jb/2004JB003010.

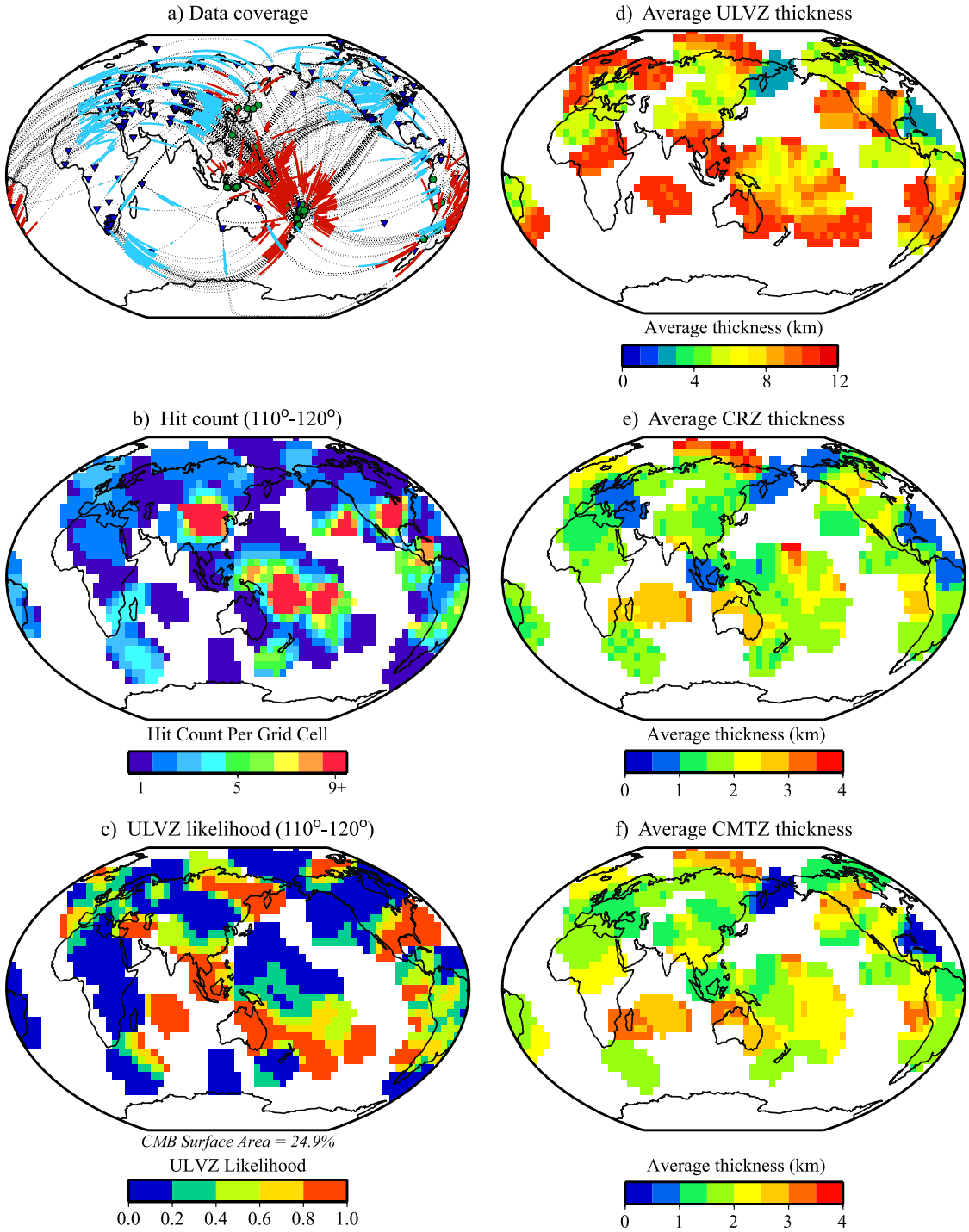

Figure 11. (a) Total data coverage. Green circles are stations, and blue triangles are events. Dotted lines show great circle paths between events and stations, and solid red and light blue lines show the P_{diff} portion of *SPdKS* and *SKPdS* on the CMB, respectively. (b) Earth divided into 5° × 5° cells colored by the number of P_{diff} segments on the CMB that pass through each grid cell. (c) Earth divided into the same grid colored by ULVZ likelihood, where a value of 1.0 signifies that all P_{diff} segments on the CMB passing through the cell had waveforms that behaved as ULVZ, and a value of 0.0 indicates that all P_{diff} segments passing through the cell had waveforms behaving as PREM. The result is shown for the most characteristic data between 110° and 120°. In italics below the projection is the total percentage of CMB surface area of grid cells with P_{diff} segments passing through them. (d–f) Average thickness for ULVZ, CRZ, and CMTZ models averaged in the same grid spacing. ULVZ model properties in Figure 11d are $\delta V_S = -15\%$, $\delta V_P = -5\%$, $\delta\rho = +5\%$. CRZ model properties in Figure 11e are $\delta V_S = -59\%$, $\delta V_P = -34\%$, $\delta\rho = +42\%$. Model thickness is only averaged for records where the model is within 5% of the best fitting model. For comparison of thickness with other ULVZ models, scaling may be applied as suggested in Table 5.

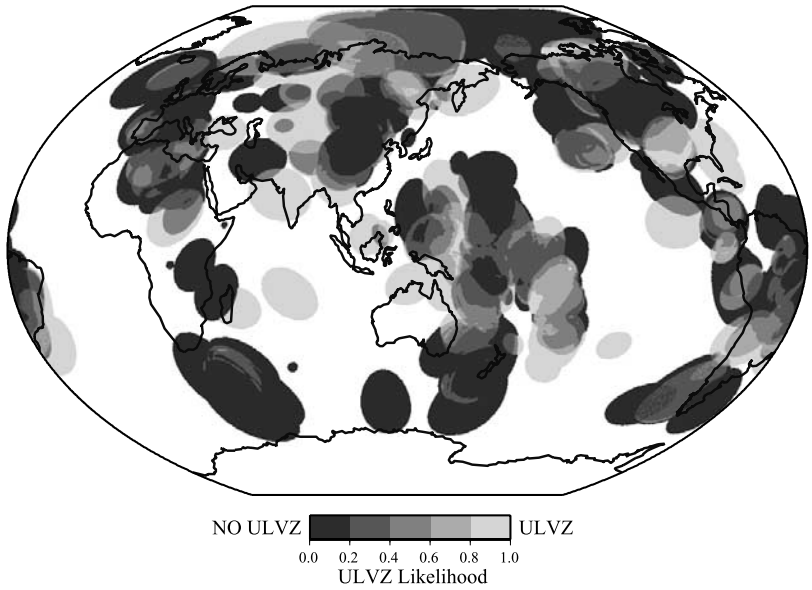

Figure 12. Fresnel zones for P_{diff} segments of *SPdKS* on the CMB shaded by ULVZ likelihood, where ULVZ likelihood is as described in Figure 11. Fresnel zones are calculated for one quarter wavelength with a dominant period of 10 s for a ULVZ model with a V_P reduction of 10%.

the south to ULVZ-like structure in the north. This finding coincides remarkably well with the likelihood transition at the southeast tip of Africa for our most constrainable data (Figure 11c). Here we only use data from one of the four events used by *Wen* [2001]. Additionally, *Helmberger et al.* [2000] suggest that ULVZ structure exists beneath Iceland and the East African Rift. Our averaging scheme does not result in the highest ULVZ likelihood (1.0) in either region but is >0.5 under Iceland and displays some evidence under the East African Rift corroborating this possibility. However, as noted above, our data coverage is sparse beneath most of Africa. Further evidence has been supplied that ULVZ structure exists under the southern Atlantic Ocean from studies of *S-ScS* travel times and waveform anomalies [*Simmons and Grand*, 2002; *Ni and Helmberger*, 2003b]. However, we have no data coverage there.

[48] As noted, seemingly conflicting results have been reported for the existence/nonexistence of ULVZs for a given region. The ULVZ likelihood approach is useful for identifying regions that display variability in solution models that often depend on the wavelength of the energy modeled (e.g., short-period versus broadband data). We stress that the exact sampling location and dominant wavelength of observation is extremely important for model determination. The likelihood map presented in Figure 11 provides a better estimation of where ULVZ structure may exist than the simple binary distributions previously presented [e.g., *Garnero et al.*, 1998].

[49] Fresnel zones of the P_{diff} segments of *SPdKS* can also be used in ULVZ map construction [*Garnero et al.*, 1998]. Figure 12 shows *SPdKS* P_{diff} Fresnel zones ($^1/_4$ wavelength, 10 s dominant period, calculated for a ULVZ model with a 10% reduction in V_P), where the shading represents ULVZ likelihood (as in Figure 11). Light shading corresponds to high likelihood of having ULVZ structure and dark shading indicates low likelihood. While using Fresnel zones are extremely useful for accommodating likely wavelengths of wave field sensitivity, caution must be taken in subsequent interpretation, because significant sub-Fresnel zone variability exists (Figure 10). This was a pitfall of the final ULVZ distribution figure of *Garnero et al.* [1998] that utilized Fresnel zones, as with Figure 12, and the spatial averaging used in Figure 11; lateral variations in boundary layer structure appear to exist at wavelengths much shorter than Fresnel zones or our grid cell sizes.

6. Discussion

[50] In this paper, we present a method to assign best fit 1-D models to high-quality broadband *SPdKS* data. Our main focus has been to identify likely regions of anomalous CMB structure. While this data set and method greatly improve our earlier efforts, several uncertainties are still present. In this section we discuss important sources of uncertainty and the relationship between likely ULVZ presence and overlying mantle heterogeneity.

6.1. Uncertainties in Mapping ULVZ Structure

[51] Perhaps the most significant uncertainty associated with *SPdKS* analyses is the difficulty in attributing anomalous *SPdKS* signals to either the *SPdKS* core entry or exit (or both) locations. This is identical to trade-offs in *PKP* precursor analyses aimed at D″ scatterer modeling [e.g., *Hedlin and Shearer*, 2000]. Some crossing paths help to reduce these uncertainties, but many regions lack any azimuthal sampling.

[52] While static displacements of the CMB do not affect our results, small-scale topography (e.g., domes) can act to focus or defocus energy and may play a significant role in perturbing *SPdKS* relative to *SKS* (or vice versa), resulting in erroneous mapping of structure. Data coverage at present is not adequate to address this issue globally. Some regional efforts (as by *Wen and Helmberger* [1998a]) may have dense enough sampling to constrain such features.

Table 5. Average CMB Layer Thickness

	Model[a]			Average Thickness, km (NR)[b]	
	$-\delta V_S$, %	$-\delta V_P$, %	$+\delta\rho$, %	PLVZ	ULVZ[c]
ULVZ	5	5	0	4.7 (214)	19.3 (59)
ULVZ	5	5	20	3.4 (210)	10.6 (73)
ULVZ	5	5	40	2.8 (208)	8.8 (79)
ULVZ	10	10	0	3.4 (208)	9.6 (74)
ULVZ	15	5	0	3.0 (209)	8.2 (62)
ULVZ	15	5	20	2.4 (203)	6.7 (75)
ULVZ	15	5	40	2.3 (190)	5.6 (78)
ULVZ	30	10	0	2.2 (189)	4.7 (68)
CRZ	86	40	78	0.5 (180)	0.9 (59)
CRZ	72	38	78	0.5 (188)	1.3 (72)
CRZ	59	34	78	0.6 (197)	1.4 (78)
CRZ	59	34	42	0.6 (206)	1.8 (81)
CRZ	59	34	7	0.8 (210)	2.4 (73)
CMTZ	NA	NA	NA	0.6 (214)	1.9 (82)

[a]Percentages are referenced to properties on the mantle side of the CMB relative to PREM.

[b]NR, total number of records for which the average was calculated and for which the specified model has a CC coefficient within 5% of the best fitting model.

[c]ULVZ represents any of the CMB boundary layer types (as in ULVZ, CRZ, and CMTZ).

[53] In most *SPdKS* modeling to date, synthetic predictions assume that *SKS* also propagates through the ULVZ structure, resulting in an *SKS* delay. For example, a 20 km thick ULVZ with a 10% δV_P reduction results in an *SKS* delay of ~0.3 s. In 1-D modeling, *SKS* travels through the ULVZ structure twice; thus a 0.6 s anomaly accumulates. If, in fact, *SKS* does not traverse any ULVZ, then a 0.6 s bias has been folded into the modeling, which amounts to an underestimation of *SPdKS* delays (because *SKS* has been artificially delayed and *SPdKS* is analyzed relative to *SKS*). This affect should only minimally affect our results because (1) most of our best fit models are thinner than this example and (2) a 0.6 s differential time error will only result in a minor mismapping of ULVZ strength. Nonetheless, future efforts need to focus beyond 1-D methods.

[54] Our modeling has assumed constant anomalous property layering (except the CMTZ models) for a single layer. More recent work has suggested multiple ULVZ layers in two localized regions: beneath the central Pacific [*Avants et al.*, 2003] and beneath North America [*Rondenay and Fischer*, 2003]. Some of our regions may entail much greater complexity than this first effort at global ULVZ characterization.

[55] Because of the various modeling trade-offs the absolute velocity reductions, density increases, or thickness cannot be constrained in this study. However, average ULVZ properties (e.g., thickness) can be pursued for specific model assumptions. Table 5 presents the average ULVZ thickness for a variety of model types. For each model we (1) extracted the best fitting thickness of that model type for every *SPdKS* observation, (2) discarded records having a CC coefficient (for that specific model) below 5% of that of the overall best fit synthetic to that observation, and (3) averaged the resulting thicknesses for all records that fulfilled requirement 2 (this was done separately for both PLVZ and ULVZ model characterizations). The average thickness is given in Table 5 with the number of qualifying records listed in parentheses to the right. It is notable that the number of qualifying records for each of the models presented is approximately equal (for either PLVZ or ULVZ), which is further indication of the modeling trade-offs. Nonetheless, several key generalizations can be made from these modeling summaries:

[56] 1. For ULVZ models, (1) doubling the velocity reduction (where $\delta V_S = \delta V_P$) results in an average ULVZ thickness roughly halved, (2) doubling the density increase reduces ULVZ thickness by roughly 20%, (3) equal δV_S and δV_P reductions have the greatest average ULVZ thickness (for the parameter space we explored with $\delta V_S = \delta V_P$), (4) for $\delta V_S = 3\delta V_P$ (representing the partial melt scenario), greater thicknesses can be achieved if the velocity reductions are relatively mild (in our model space the thickest partially molten ULVZ (~8 km) occurs for $\delta V_S = -15\%$, $\delta V_P = -5\%$, $\delta\rho = +0\%$), and (5) increasing velocity reductions or density increases for $\delta V_S = 3\delta V_P$, and the average ULVZ thickness significantly decreases, e.g., <5 km average thickness results for $\delta V_S = -30\%$, $\delta V_P = -10\%$, $\delta\rho = +0\%$.

[57] 2. For CRZ models, increasing V_S or ρ decreases CRZ thickness.

[58] 3. For CMTZ models, the average thickness is <2.0 km.

[59] If we assume a specific model type (e.g., as in Table 5), boundary layer distribution and thickness maps can be constructed. Figure 11d shows the average thickness of one ULVZ model ($\delta V_S = -15\%$, $\delta V_P = -5\%$, $\delta\rho = +5\%$), averaged onto $5^\circ \times 5^\circ$ grid cells. Additionally, Figures 11e and 11f show the average thickness of one CRZ model ($\delta V_S = -59\%$, $\delta V_P = -34\%$, $\delta\rho = +42\%$) and for CMTZ. These maps are produced by averaging best fitting thicknesses in each grid cell for all data characterized by a CC coefficient within 5% of the best fitting record (for that specific model). Figure 11 does not include thickness averages for waveforms classified as PLVZ and thus represents a maximum thickness for the sampled regions. Interestingly, thick ULVZ is exhibited (Figure 11d) in the East African Rift area and under Iceland, as suggested by *Helmberger et al.* [2000], where only moderate ULVZ likelihood was suggested (Figure 11c). Approximate thicknesses for other ULVZ model properties may be estimated to first order from the present map and Table 5. For example, for an ULVZ model with $\delta V_S = -30\%$, $\delta V_P = -10\%$, and $\delta\rho = +0\%$, the average thickness of each cell would be reduced by approximately half. We note that our complete list of model parameters, cross-correlation coefficients, and ULVZ likelihood maps are available in ASCII format in the auxiliary material.

6.2. Relating ULVZ and Mantle Heterogeneity

[60] We have compared these likelihood maps to several *P* and *S* wave tomography models [*Boschi and Dziewonski*, 1999; *Megnin and Romanowicz*, 2000; *Ritsema and van Heijst*, 2000; *Gu et al.*, 2001; *Kárason and van der Hilst*, 2001; *Zhao*, 2001; *Grand*, 2002]. However, there is no significant correlation between strong ULVZ likelihood and lowermost mantle velocities from these tomographic models. This may be expected owing to the source-receiver ambiguity of *SPdKS*. For example, tomographic models of

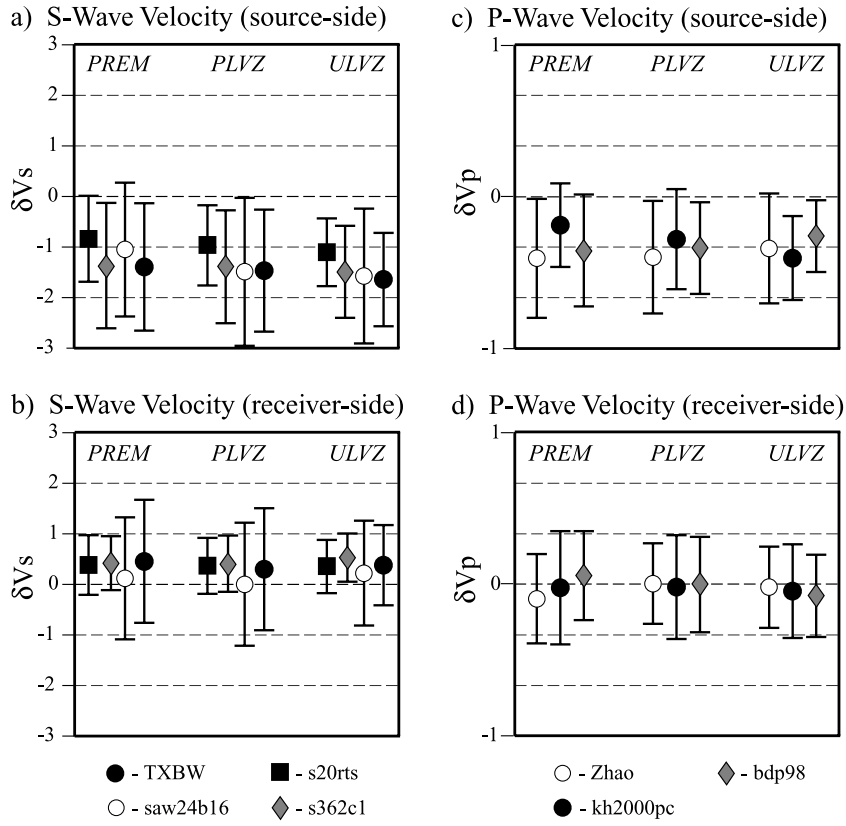

Figure 13. Comparison between *SPdKS* source- and receiver-side arcs with four *S* wave and three *P* wave tomography models. The comparison is carried out for all data with source-receiver distances between 110° and 120°. For each tomographic model the average and standard deviation of the lowest velocity encountered along a P_{diff} segment are shown. Individual model results are grouped into categories of PREM, PLVZ, and ULVZ waveform classifications. *S* wave models are TXBW [*Grand*, 2002], saw24b16 [*Megnin and Romanowicz*, 2000], s20rts [*Ritsema and van Heijst*, 2000], and s362c1 [*Gu et al.*, 2001]. *P wave* models are kh2000pc [*Kárason and van der Hilst*, 2001], Zhao [*Zhao*, 2001], and bdp98 [*Boschi and Dziewonski*, 1999].

shear wave velocity display strong degree 2 heterogeneity, with low velocities below the Pacific and Africa and high velocities in the circum-Pacific region. All of our records originate in sources along deep subduction zones circling the Pacific. For example, a record originating in the Fiji-Tonga subduction complex and recorded in North America or Asia may have P_{diff} segments on the source side, encountering low shear wave velocities in the Pacific and high shear wave velocities on the receiver side in the North America or Asian regions. Because we cannot distinguish between source- or receiver-side ULVZ anomalies, ULVZ likelihood estimations in both locales are affected. This causes an averaging effect in comparing likelihood to tomography results. Thus, while ULVZ structure may strongly relate to lowermost mantle velocities, the correlation between our likelihood maps and lowermost mantle velocities may be blurred because of the source versus receiver side of path ambiguity (which is explored in greater detail in section 6.3). As data coverage and crossing path sampling increases, future efforts will better minimize uncertainties due to the source-receiver ambiguity in *SPdKS* modeling.

[61] However, there is a correlation with tomographic models of shear wave velocity and the source-side P_{diff} segments used in this study. For each record in our study we have determined the lowest velocity encountered on each P_{diff} segment for both source- and receiver-side arcs for four models of *S* wave tomography [*Megnin and Romanowicz*, 2000; *Ritsema and van Heijst*, 2000; *Gu et al.*, 2001; *Grand*, 2002] and three models of *P wave* tomography [*Boschi and Dziewonski*, 1999; *Kárason and van der Hilst*, 2001; *Zhao*, 2001]. The most notable correlation occurs for P_{diff} segments from data in the distance range of 110°–120°. Figure 13 shows averages of the lowest tomographic velocities along either source- or receiver-side P_{diff} segments for the different model classifications of PREM, PLVZ, or ULVZ (ELVZ waveforms are combined with the ULVZ waveforms for this analysis). For both the *P* and *S* wave models the lowest velocities encountered by the *SPdKS* P_{diff} segments are predominantly on the source side and approximately zero on the receiver side of the path. No clear trend is found between average *P* wave velocities and *SPdKS* anomalies (i.e., PREM, PLVZ, or ULVZ data), with the exception of model kh2000pc [*Kárason and van der Hilst*, 2001]. For model kh2000pc the P_{diff} segments on the source side typically encounter higher velocities for PREM than for PLVZ (slightly lower), and for ULVZ (lower yet), than for

the receiver side of the path. This trend is apparent for all *S* wave models analyzed. That is, considering the source-side segments for all *S* wave models, the PREM-like waveforms encounter the higher velocities on average than those classified as ULVZ. Also, PLVZ-classified waveforms on average encounter *S* wave velocities in between PREM and ULVZ data. The velocity averages for receiver-side P_{diff} segments do not show any apparent trend relating to our waveform classification.

[62] As our inferred structure varies on rather small length scales, we have attempted to make our comparisons with global structures with the shortest-wavelength variations. However, no apparent agreement in correlation is evident in the *P* wave models, which may be related to the general disagreement between the models, and indicate a necessity to utilize models specifically aimed at determining D″ structure or at more detailed regional maps [e.g., *Valenzuela et al.*, 2000; *Tkalčić et al.*, 2002; *Tkalčić and Romanowicz*, 2002]. Of the *P* wave models analyzed here, only kh2000pc utilizes P_{diff}, which may result in the better correlation to the ULVZ results than for the other *P* structures. As longer distance records may inappropriately be classified as PREM-like (see section 5.2), correspondence of low tomographically derived V_S and source-side P_{diff} arcs is less apparent when using our entire data set (in comparison to using the 110°–120° subset). As expected, more PREM-like averages of encountered tomographic velocities result from inclusion of the largest distance data (i.e., >120°). Because the main source region of events used in this study lie in the southwest Pacific, and the majority of receiver locations are in eastern Asia and North America (Figure 11a) rays from the same event are more likely to sample bins on the source side, whereas bins nearest the receiver side are more likely to be sampled by rays from a wide range of events. Hence the limited coverage enforced by source-receiver geometry inadequacy may introduce a geographical bias in our low V_S and source-side P_{diff} arc correspondence.

6.3. *SPdKS* Ray Path Uncertainties

[63] In our one-dimensional modeling efforts, boundary layer structure exists at both the source and receiver sides of the *SPdKS* path. However, ULVZ structure may be confined to only one side and may only partially interact with the P_{diff} segments on that side. Figure 14 illustrates three different ULVZ localizations on the source side. In Figure 14a the *SPdKS* P_{diff} segment initiates, propagates, and then exits completely within the ULVZ (solid line ray path). For reference, the dashed line indicates the ray path for PREM. Of first note, the critical angle ($\theta^{u}_{c,1}$) for *ScP* converting to a P_{diff} segment increases for a ULVZ, as compared to that for PREM ($\theta^{p}_{c,1}$). All diffracted waves within a ULVZ exit into the core at the same model-dependent critical angle ($\theta^{u}_{c,2}$). The P_{diff} inception location (i.e., where *P* diffraction initiates) is closer to the earthquake source for the ULVZ model than for PREM, resulting in longer diffraction distances (to reach the same receiver).

[64] Figure 14b depicts the situation where P_{diff} initiates in PREM mantle and then propagates in a ULVZ before diving into the core. In this case, the diffraction length is larger than for pure PREM paths. The opposite geometry is also possible, that is, the P_{diff} inception can occur in an isolated ULVZ, exit the ULVZ into PREM-like mantle, and then dive into the core from PREM mantle. It is also possible the P_{diff} passes through one or several ULVZ structures of a much smaller scale than the P_{diff} arcs. In this case, travel time anomalies associated with *SPdKS* may

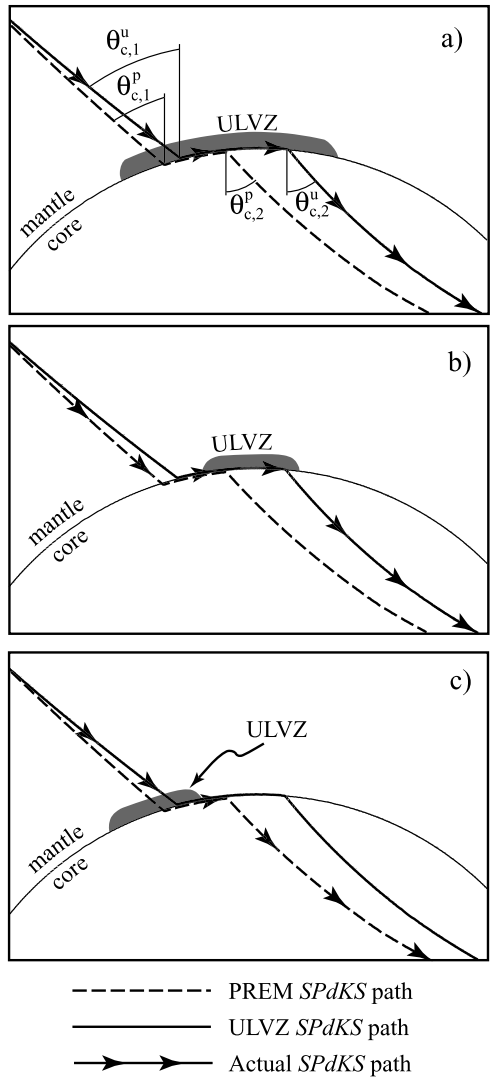

Figure 14. Source-side *SPdKS* ray path geometry for three different possibilities of ULVZ location. The dashed line indicates the path *SPdKS* would take if the mantle were purely PREM, and the solid line indicates the path *SPdKS* would take if there existed a 30 km thick ULVZ ($\delta V_S = -15\%$, $\delta V_P = -5\%$, $\delta\rho = +0\%$) at the base of the mantle. Arrows outline the actual path *SPdKS* takes. In Figure 14a the ray path encounters the ULVZ and becomes critical at an angle of $\theta^{u}_{c,1}$. The P_{diff} path continues through the ULVZ and exits at the same critical angle $\theta^{u}_{c,2}$. If the ULVZ did not exist, the ray path would follow the PREM prediction and become critical at angle $\theta^{p}_{c,1}$ with the P_{diff} path also exiting at that angle ($\theta^{p}_{c,2}$). In Figure 14b, no ULVZ exists at the inception point of P_{diff} and becomes critical at angle $\theta^{p}_{c,1}$. However, P_{diff} encounters the ULVZ along its path and thus exits at the critical angle for the ULVZ model $\theta^{u}_{c,2}$. In Figure 14c the situation is reversed from Figure 14b. The geometry of the ray paths was calculated for a source-receiver distance of 115° and a source depth of 500 km.

be abrogated by wave front healing making their existence difficult to establish.

6.4. Two- and Three-Dimensional Synthetics

[65] In the three cases of Figure 14, the length of diffraction, as well as the P_{diff} inception and termination locations vary significantly. Synthetic waveforms that account for structure in two or three dimensions are desired (e.g., by utilizing methods such as presented by *Igel and Weber* [1996], *Helmberger et al.* [1996], and *Wen and Helmberger* [1998a]). *Helmberger et al.* [1996] studied the effects of two-sided structures, with PREM-like mantle on one side and a ULVZ structure on the opposite side of the *SPdKS* path. Two distinct waveform effects (relative to 1-D modeling) were noticed: (1) a decrease in *SPdKS* amplitude near 110°–112° occurs, as the anomalous signal comes from only half of the geometric path, and (2) at larger distances, two distinct arrivals are apparent, one for *SPdKS* and *SKPdS*. The source versus receiver side of path ambiguity is nevertheless still present.

6.5. Other Considerations

[66] A significant amount of waveforms have been characterized as PLVZ, which raises the possibility that a thin (<5 km) ULVZ structure may exist throughout much of Earth's D″ layer. *Williams and Garnero* [1996] suggested that if ULVZs are of partial melt origin, they might arise if the geotherm is close to the solidus of silicate mantle. For this case, ULVZs should be a global feature (as the CMB should be isothermal) but could be very thin in colder regions. At present, it may be difficult to detect such a possibility. Even with array methods, it is difficult to resolve "typical" ULVZ boundary layering (e.g., $\delta V_S = \delta V_P = -10\%$) much thinner than ~3 km [e.g., *Rost and Revenaugh*, 2003]. A gradational top to the ULVZ may further hinder ULVZ detection in such studies. However, one may expect greater *SPdKS* delays in higher-frequency data as P_{diff} may be more efficiently trapped inside a ULVZ. Thus, using shorter-period data may prove useful in future characterizations of ULVZ structure.

[67] As global coverage increases, particularly through combining results of the other important ULVZ probes, comparisons between better constrained global ULVZ maps and other related phenomena will be important, such as possible preferred magnetic field reversal paths [e.g., *Laj et al.*, 1991; *Brito et al.*, 1999; *Kutzner and Christensen*, 2004], or the geographic distribution of hot spots [e.g., *Williams et al.*, 1998].

7. Conclusions

[68] We have investigated anomalous boundary layer structure at the core-mantle boundary using a global set of broadband *SKS* and *SPdKS* waves. In an attempt to circumvent the strong modeling trade-offs we have produced ULVZ likelihood maps, inferring regional patterns in ULVZ structure. The southwest Pacific, Central America, Indian Ocean, and northeast Asia regions indicate the highest likelihood of ULVZ existence, whereas the North America, central east Asia, and Africa regions display the lowest likelihood. Although there exists ambiguity over whether anomalous boundary layer structure exists on the source or receiver side of the *SPdKS* paths, there exists an apparent correlation with lower mantle *S* wave velocity as inferred from tomography. This finding is consistent with ULVZ structure predominantly existing on the source side of *SPdKS* paths. Additionally, broadband *SPdKS* data are determined to be most sensitive to boundary layer structure in the distance range of 110°–115°. We observe very short scale heterogeneity, with P_{diff} segments separated by tens of kilometers, consistent with past studies. A partial melt origin to ULVZs implies a global average ULVZ thickness of <10 km for $\delta V_S = -15\%$, $\delta V_P = -5\%$, and $\delta\rho = +0\%$. Stronger velocity reductions or density increases results in an even thinner ULVZ. Better constraint on structural specifics is necessary; combining *SPdKS* analyses with other ULVZ probes (both short-period and broadband) in addition to modeling waveforms with higher dimensional methods will greatly advance our ability to constrain ULVZ layer properties and geographical distribution (including the possibility of an ubiquitous ULVZ layer).

[69] **Acknowledgments.** The authors thank T. Lay and S. Rost for useful discussions, the IRIS, ORPHEUS, and CNSN data agencies for the broadband data, and M. Fouch for helping with data processing. The authors also thank J. Revenaugh, S. Rondenay, and H. Tkalčić for constructive review and suggestions. M.T. and E.G. were partially supported by NSF grants EAR-9905710, and EAR-0135119. Most figures were generated using the Generic Mapping Tools freeware package [*Wessel and Smith*, 1998]. Actual waveform data used in this study are available at http://ulvz.asu.edu.

References

Avants, M. S., T. Lay, and E. Garnero (2003), Determining shear velocity structure of ULVZs using stacked ScS data, *Eos Trans. AGU*, *84*(46), Fall Meet. Suppl., Abstract U41C-02.

Berryman, J. G. (2000), Seismic velocity decrement ratios for regions of partial melt in the lower mantle, *Geophys. Res. Lett.*, *27*(3), 421–424.

Boschi, L., and A. M. Dziewonski (1999), High- and low-resolution images of the Earth's mantle: Implications of different approaches to tomographic modeling, *J. Geophys. Res.*, *104*(B11), 25,567–25,594.

Bowers, D., D. A. McCormack, and D. S. Sharrock (2000), Observations of *PKP* (*DF*) and *PKP* (*BC*) across the United Kingdom: Implications for studies of attenuation in the Earth's core, *Geophys. J. Int.*, *140*(2), 374–384.

Bowin, C. (1986), Topography at the core mantle boundary, *Geophys. Res. Lett.*, *13*(13), 1513–1516.

Brito, D., J. Aurnou, and P. Olson (1999), Can heterogeneous core-mantle electromagnetic coupling control geomagnetic reversals?, *Phys. Earth Planet. Inter.*, *112*(3–4), 159–170.

Buffett, B. A., E. J. Garnero, and R. Jeanloz (2000), Sediments at the top of Earth's core, *Science*, *290*(5495), 1338–1342.

Castle, J. C., and R. D. van der Hilst (2000), The core-mantle boundary under the Gulf of Alaska: No ULVZ for shear waves, *Earth Planet. Sci. Lett.*, *176*(3–4), 311–321.

Choy, G. L., V. F. Cormier, R. Kind, G. Muller, and P. G. Richards (1980), A comparison of synthetic seismograms of core phases generated by the full-wave theory and by the reflectivity method, *Geophys. J. R. Astron. Soc.*, *61*(1), 21–39.

Creager, K. C., and T. H. Jordan (1986), Aspherical structure of the core-mantle boundary from *PKP* travel-times, *Geophys. Res. Lett.*, *13*(13), 1497–1500.

Doornbos, D. J. (1983), Present seismic evidence for a boundary-layer at the base of the mantle, *J. Geophys. Res.*, *88*(B4), 3498–3505.

Doornbos, D. J., and T. Hilton (1989), Models of the core-mantle boundary and the travel-times of internally reflected core phases, *J. Geophys. Res.*, *94*(B11), 15,741–15,751.

Dziewonski, A. M., and D. L. Anderson (1981), Preliminary reference Earth model, *Phys. Earth Planet. Inter.*, *25*(4), 297–356.

Earle, P. S., and P. M. Shearer (1997), Observations of *PKKP* precursors used to estimate small-scale topography on the core-mantle boundary, *Science*, *277*(5326), 667–670.

Fisher, J. L., M. E. Wysession, and K. M. Fischer (2003), Small-scale lateral variations in D″ attenuation and velocity structure, *Geophys. Res. Lett.*, *30*(8), 1435, doi:10.1029/2002GL016179.

Fuchs, K., and G. Müller (1971), Computation of synthetic seismograms with reflectivity method and comparison with observations, *Geophys. J. R. Astron. Soc.*, *23*(4), 417–433.

Garcia, R., and A. Souriau (2000), Amplitude of the core-mantle boundary topography estimated by stochastic analysis of core phases, *Phys. Earth Planet. Inter.*, *117*(1–4), 345–359.

Garnero, E. J. (2000), Heterogeneity of the lowermost mantle, *Annu. Rev. Earth Planet. Sci.*, *28*, 509–537.

Garnero, E. J., and D. V. Helmberger (1995), A very slow basal layer underlying large-scale low-velocity anomalies in the lower mantle beneath the Pacific: Evidence from core phases, *Phys. Earth Planet. Inter.*, *91*(1–3), 161–176.

Garnero, E. J., and D. V. Helmberger (1996), Seismic detection of a thin laterally varying boundary layer at the base of the mantle beneath the central-Pacific, *Geophys. Res. Lett.*, *23*(9), 977–980.

Garnero, E. J., and D. V. Helmberger (1998), Further structural constraints and uncertainties of a thin laterally varying ultralow-velocity layer at the base of the mantle, *J. Geophys. Res.*, *103*(B6), 12,495–12,509.

Garnero, E. J., and R. Jeanloz (2000a), Fuzzy patches on the Earth's core-mantle boundary?, *Geophys. Res. Lett.*, *27*(17), 2777–2780.

Garnero, E. J., and R. Jeanloz (2000b), Geophysics: Earth's enigmatic interface, *Science*, *289*(5476), 70–71.

Garnero, E. J., and J. E. Vidale (1999), *ScP*, a probe of ultralow velocity zones at the base of the mantle, *Geophys. Res. Lett.*, *26*(3), 377–380.

Garnero, E. J., S. P. Grand, and D. V. Helmberger (1993), Low *P*-wave velocity at the base of the mantle, *Geophys. Res. Lett.*, *20*(17), 1843–1846.

Garnero, E., J. Revenaugh, Q. Williams, T. Lay, and L. H. Kellogg (1998), Ultralow velocity zone at the core-mantle boundary, in *The Core-Mantle Boundary Region*, *Geodyn. Ser.*, vol. 28, edited by M. Gurnis et al., pp. 319–334, AGU, Washington, D. C.

Glatzmaier, G. A., R. S. Coe, L. Hongre, and P. H. Roberts (1999), The role of the Earth's mantle in controlling the frequency of geomagnetic reversals, *Nature*, *401*(6756), 885–890.

Goldstein, P., D. Dodge, and M. Firpo (1999), SAC2000: Signal processing and analysis tools for seismologists and engineers, in *International Handbook of Earthquake and Engineering Seismology*, *Part B*, *Int. Geophys. Ser.*, vol. 81, edited by W. H. K. Lee et al., pp. 1613–1614, Academic, San Diego, Calif.

Grand, S. P. (2002), Mantle shear-wave tomography and the fate of subducted slabs, *Philos. Trans. R. Soc. London, Ser. A*, *360*(1800), 2475–2491.

Grand, S. P., R. D. van der Hilst, and S. Widiyantoro (1997), Global seismic tomography: A snapshot of convection in the Earth, *GSA Today*, *7*(4), 1–7.

Gu, Y. J., A. M. Dziewonski, W. J. Su, and G. Ekstrom (2001), Models of the mantle shear velocity and discontinuities in the pattern of lateral heterogeneities, *J. Geophys. Res.*, *106*(B6), 11,169–11,199.

Hager, B. H., R. W. Clayton, M. A. Richards, R. P. Comer, and A. M. Dziewonski (1985), Lower mantle heterogeneity, dynamic topography and the geoid, *Nature*, *313*(6003), 541–546.

Havens, E., and J. Revenaugh (2001), A broadband seismic study of the lowermost mantle beneath Mexico: Constraints on ultralow-velocity zone elasticity and density, *J. Geophys. Res.*, *106*(B12), 30,809–30,820.

Hedlin, M. A. H., and P. M. Shearer (2000), An analysis of large-scale variations in small-scale mantle heterogeneity using Global Seismographic Network recordings of precursors to *PKP*, *J. Geophys. Res.*, *105*(B6), 13,655–13,673.

Helmberger, D. V., E. J. Garnero, and X. Ding (1996), Modeling two-dimensional structure at the core-mantle boundary, *J. Geophys. Res.*, *101*(B6), 13,963–13,972.

Helmberger, D. V., L. Wen, and X. Ding (1998), Seismic evidence that the source of the Iceland hotspot lies at the core-mantle boundary, *Nature*, *396*(6708), 251–255.

Helmberger, D., S. D. Ni, L. X. Wen, and J. Ritsema (2000), Seismic evidence for ultralow-velocity zones beneath Africa and eastern Atlantic, *J. Geophys. Res.*, *105*(B10), 23,865–23,878.

Hide, R., R. W. Clayton, B. H. Hager, M. A. Spieth, and C. V. Voorhies (1993), Topographic core-mantle coupling and fluctuations in the Earth's rotation, in *Dynamics of the Earth's Deep Interior and Earth Rotation*, *Geophys. Monogr. Ser.*, vol. 72, edited by J.-L. Mouel, D. E. Smylie, and T. Herring, pp. 113–125, AGU, Washington, D. C.

Igel, H., and M. Weber (1996), *P-SV* wave propagation in the Earth's mantle using finite differences: Application to heterogeneous lowermost mantle structure, *Geophys. Res. Lett.*, *23*(5), 415–418.

Kárason, H., and R. D. van der Hilst (2001), Tomographic imaging of the lowermost mantle with differential times of refracted and diffracted core phases (*PKP*, P_{diff}), *J. Geophys. Res.*, *106*(B4), 6569–6587.

Kohler, M. D., J. E. Vidale, and P. M. Davis (1997), Complex scattering within D″ observed on the very dense Los Angeles region seismic experiment passive array, *Geophys. Res. Lett.*, *24*(15), 1855–1858.

Kutzner, C., and U. R. Christensen (2004), Simulated geomagnetic reversals and preferred VGP paths, *Geophys. J. Int.*, *157*, 1105–1118.

Laj, C., A. Mazaud, M. Fuller, R. Weeks, and E. Herrero-Bervera (1991), Lateral variations at the core-mantle boundary revealed by geomagnetic reversal paths?, *Nature*, *351*, 447.

Luo, S. N., S. D. Ni, and D. V. Helmberger (2001), Evidence for a sharp lateral variation of velocity at the core-mantle boundary from multipathed *PKP*ab, *Earth Planet. Sci. Lett.*, *189*(3–4), 155–164.

Manga, M., and R. Jeanloz (1996), Implications of a metal-bearing chemical boundary layer in D″ for mantle dynamics, *Geophys. Res. Lett.*, *23*(22), 3091–3094.

Masters, G., G. Laske, H. Bolton, and A. M. Dziewonski (2000), The relative behavior of shear velocity, bulk sound speed, and compressional velocity in the mantle: Implications for chemical and thermal structure, in *Earth's Deep Interior: Mineral Physics and Tomography From the Atomic to the Global Scale*, Geophys. Monogr. Ser., vol. 117, edited by S. Karato et al., pp. 63–87, AGU, Washington D. C.

Megnin, C., and B. Romanowicz (2000), The three-dimensional shear velocity structure of the mantle from the inversion of body, surface and higher-mode waveforms, *Geophys. J. Int.*, *143*(3), 709–728.

Montelli, R., G. Nolet, F. A. Dahlen, G. Masters, E. R. Engdahl, and S. H. Hung (2004), Finite-frequency tomography reveals a variety of plumes in the mantle, *Science*, *303*(5656), 338–343.

Morelli, A., and A. M. Dziewonski (1987), Topography of the core-mantle boundary and lateral homogeneity of the liquid core, *Nature*, *325*(6106), 678–683.

Mori, J., and D. V. Helmberger (1995), Localized boundary-layer below the mid-Pacific velocity anomaly identified from a *PcP* precursor, *J. Geophys. Res.*, *100*(B10), 20,359–20,365.

Müller, G. (1985), The reflectivity method—A tutorial, *Z. Geophys.*, *58*(1–3), 153–174.

Ni, S., and D. V. Helmberger (2001a), Probing an ultra-low velocity zone at the core mantle boundary with *P* and *S* waves, *Geophys. Res. Lett.*, *28*(12), 2345–2348.

Ni, S. D., and D. V. Helmberger (2001b), Horizontal transition from fast to slow structures at the core- mantle boundary; South Atlantic, *Earth Planet. Sci. Lett.*, *187*(3–4), 301–310.

Ni, S. D., and D. V. Helmberger (2003a), Seismological constraints on the South African superplume; could be the oldest distinct structure on Earth, *Earth Planet. Sci. Lett.*, *206*(1–2), 119–131.

Ni, S., and D. V. Helmberger (2003b), Ridge-like lower mantle structure beneath South Africa, *J. Geophys. Res.*, *108*(B2), 2094, doi:10.1029/2001JB001545.

Niu, F. L., and L. X. Wen (2001), Strong seismic scatterers near the core-mantle boundary west of Mexico, *Geophys. Res. Lett.*, *28*(18), 3557–3560.

Persh, S. E., J. E. Vidale, and P. S. Earle (2001), Absence of short-period ULVZ precursors to *PcP* and *ScP* from two regions of the CMB, *Geophys. Res. Lett.*, *28*(2), 387–390.

Reasoner, C., and J. Revenaugh (2000), *ScP* constraints on ultralow-velocity zone density and gradient thickness beneath the Pacific, *J. Geophys. Res.*, *105*(B12), 28,173–28,182.

Revenaugh, J., and R. Meyer (1997), Seismic evidence of partial melt within a possibly ubiquitous low-velocity layer at the base of the mantle, *Science*, *277*(5326), 670–673.

Ritsema, J., and H.-J. van Heijst (2000), Seismic imaging of structural heterogeneity in Earth's mantle: Evidence for large-scale mantle flow, *Sci. Progress*, *83*, 243–259.

Rodgers, A., and J. Wahr (1993), Inference of core-mantle boundary topography from Isc *PCP* and *PKP* travel-times, *Geophys. J. Int.*, *115*(3), 991–1011.

Rondenay, S., and K. M. Fischer (2003), Constraints on localized core-mantle boundary structure from multichannel, broadband *SKS* coda analysis, *J. Geophys. Res.*, *108*(B11), 2537, doi:10.1029/2003JB002518.

Rost, S., and J. Revenaugh (2001), Seismic detection of rigid zones at the top of the core, *Science*, *294*(5548), 1911–1914.

Rost, S., and J. Revenaugh (2003), Small-scale ultralow-velocity zone structure imaged by *ScP*, *J. Geophys. Res.*, *108*(B1), 2056, doi:10.1029/2001JB001627.

Shearer, P. M., M. A. H. Hedlin, and P. S. Earle (1998), *PKP* and *PKKP* precursor observations: Implications for the small-scale structure of the deep mantle and core, in *The Core-Mantle Boundary Region*, *Geodyn. Ser.*, vol. 28, edited by M. Gurnis et al., pp. 37–55, AGU, Washington, D. C.

Simmons, N. A., and S. P. Grand (2002), Partial melting in the deepest mantle, *Geophys. Res. Lett.*, *29*(11), 1552, doi:10.1029/2001GL013716.

Sleep, N. H. (1990), Hotspots and mantle plumes: Some phenomenology, *J. Geophys. Res.*, *95*(B5), 6715–6736.

Steinberger, B. (2000), Plumes in a convecting mantle: Models and observations for individual hotspots, *J. Geophys. Res.*, *105*(B5), 11,127–11,152.

Stutzmann, E., L. Vinnik, A. Ferreira, and S. Singh (2000), Constraint on the *S*-wave velocity at the base of the mantle, *Geophys. Res. Lett.*, *27*(11), 1571–1574.

Sze, E. K. M., and R. D. van der Hilst (2003), Core mantle boundary topography from short period *PcP*, *PKP*, and *PKKP* data, *Phys. Earth Planet. Inter.*, *135*(1), 27–46.

Thomas, C., M. Weber, C. W. Wicks, and F. Scherbaum (1999), Small scatterers in the lower mantle observed at German broadband arrays, *J. Geophys. Res.*, *104*(B7), 15,073–15,088.

Thorne, M., E. Garnero, and S. Grand (2004), Geographic correlation between hot spots and deep mantle lateral shear-wave velocity gradients, *Phys. Earth Planet. Inter.*, *146*, 47–63.

Tkalčić, H., and B. Romanowicz (2002), Short scale heterogeneity in the lowermost mantle: Insights from *PcP-P* and *ScS-S* data, *Earth Planet. Sci. Lett.*, *201*(1), 57–68.

Tkalčić, H., B. Romanowicz, and N. Houy (2002), Constraints on D″ structure using *PKP* (AB-DF), *PKP* (BC-DF) and *PcP-P* traveltime data from broad-band records, *Geophys. J. Int.*, *148*, 599–616.

Valenzuela, R. W., M. E. Wysession, M. O. Neustadt, and J. L. Butler (2000), Lateral variations at the base of the mantle from profiles of digital Sdiff data, *J. Geophys. Res.*, *105*(B3), 6201–6220.

Vidale, J. E., and H. M. Benz (1992), A sharp and flat section of the core mantle boundary, *Nature*, *359*(6396), 627–629.

Vidale, J. E., and M. A. H. Hedlin (1998), Evidence for partial melt at the core-mantle boundary north Tonga from the strong scattering of seismic waves, *Nature*, *391*(6668), 682–685.

Wen, L. X. (2000), Intense seismic scattering near the Earth's core-mantle boundary beneath the Comoros hotspot, *Geophys. Res. Lett.*, *27*(22), 3627–3630.

Wen, L. X. (2001), Seismic evidence for a rapidly varying compositional anomaly at the base of the Earth's mantle beneath the Indian Ocean, *Earth Planet. Sci. Lett.*, *194*(1–2), 83–95.

Wen, L. X., and D. V. Helmberger (1998a), A two-dimensional *P-SV* hybrid method and its application to modeling localized structures near the core-mantle boundary, *J. Geophys. Res.*, *103*(B8), 17,901–17,918.

Wen, L. X., and D. V. Helmberger (1998b), Ultra-low velocity zones near the core-mantle boundary from broadband *PKP* precursors, *Science*, *279*(5357), 1701–1703.

Wessel, P., and W. H. F. Smith (1998), New, improved version of the Generic Mapping Tools released, *Eos Trans. AGU*, *79*, 579.

Williams, Q., and E. J. Garnero (1996), Seismic evidence for partial melt at the base of Earth's mantle, *Science*, *273*(5281), 1528–1530.

Williams, Q., J. Revenaugh, and E. Garnero (1998), A correlation between ultra-low basal velocities in the mantle and hot spots, *Science*, *281*(5376), 546–549.

Wysession, M. E., K. M. Fischer, G. I. Al-eqabi, P. J. Shore, and I. Gurari (2001), Using MOMA broadband array *ScS-S* data to image smaller-scale structures at the base of the mantle, *Geophys. Res. Lett.*, *28*(5), 867–870.

Zerr, A., A. Diegeler, and R. Boehler (1998), Solidus of Earth's deep mantle, *Science*, *281*(5374), 243–246.

Zhao, D. (2001), Seismic structure and origin of hotspots and mantle plumes, *Earth Planet. Sci. Lett.*, *192*(3), 251–265.

E. J. Garnero and M. S. Thorne, Department of Geological Sciences, Arizona State University, Box 871404, Tempe, AZ 85287-1404, USA. (garnero@asu.edu; mthorne@asu.edu)